Achieving ultra-stable and superior electricity generation by integrating transistor-like design with lubricant armor

Yuxin Song,[1,5] Wanghuai Xu,[1,5] Yuan Liu,[4,5] Huanxi Zheng,[1] Miaomiao Cui,[1] Yongsen Zhou,[1] Baoping Zhang,[1] Xiantong Yan,[1] Lili Wang,[1] Pengyu Li,[1] Xiaote Xu,[1] Zhengbao Yang,[1] and Zuankai Wang[1,2,3,*]

*Correspondence: zuanwang@cityu.edu.hk

Received: June 17, 2022; Accepted: August 8, 2022; Published Online: August 11, 2022; https://doi.org/10.1016/j.xinn.2022.100301

GRAPHICAL ABSTRACT

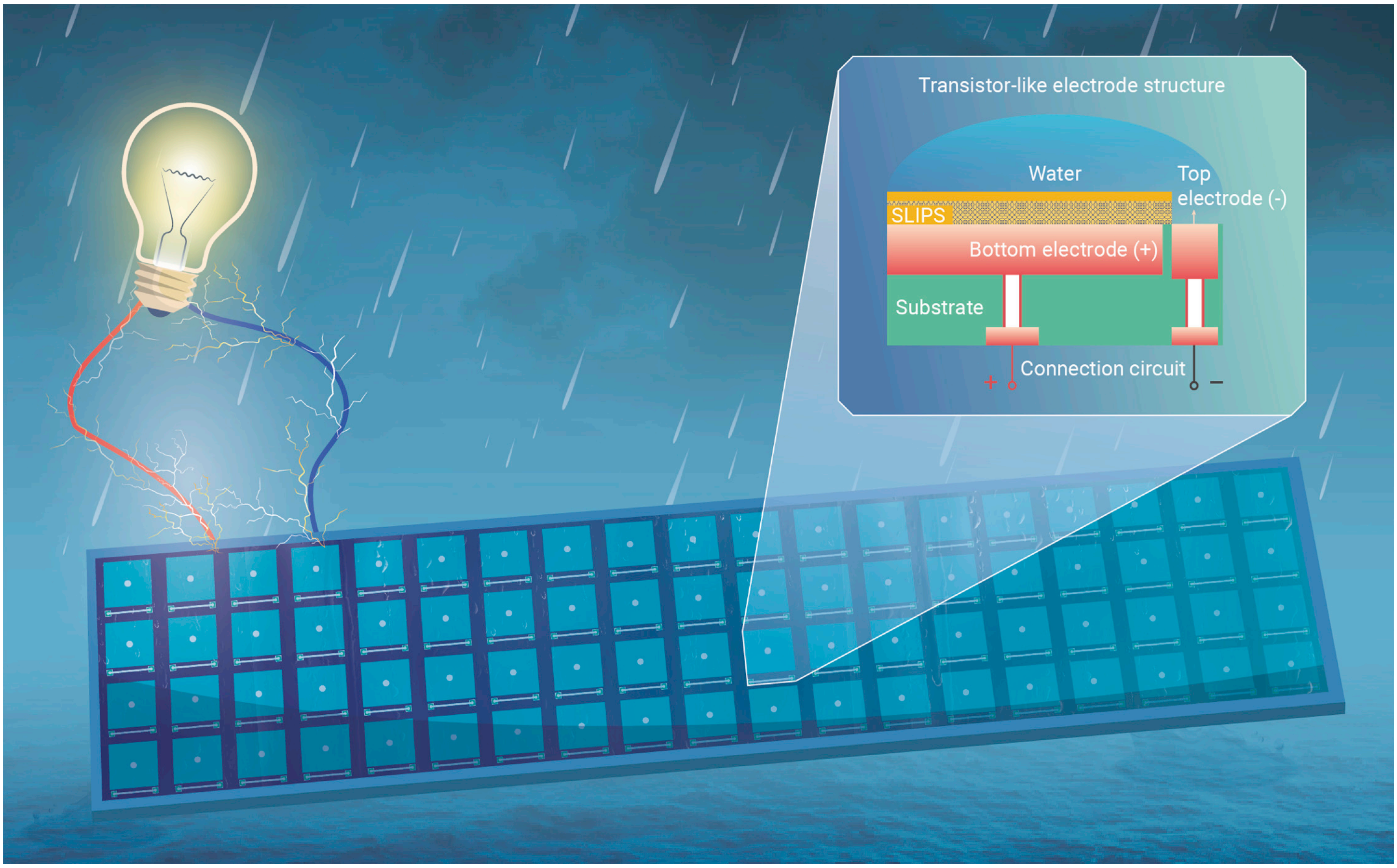

PUBLIC SUMMARY

- A lubricant-armored transistor-like electricity generator is proposed
- The transistor-like electrode architecture causes high electrical output
- The lubricant armor ensures stable performance in extreme environments
- The design is scalable in manufacturing and suitable for facile integration

Achieving ultra-stable and superior electricity generation by integrating transistor-like design with lubricant armor

Yuxin Song,[1,5] **Wanghuai Xu,**[1,5] **Yuan Liu,**[4,5] **Huanxi Zheng,**[1] **Miaomiao Cui,**[1] **Yongsen Zhou,**[1] **Baoping Zhang,**[1] **Xiantong Yan,**[1] **Lili Wang,**[1] **Pengyu Li,**[1] **Xiaote Xu,**[1] **Zhengbao Yang,**[1] **and Zuankai Wang**[1,2,3,*]

[1]Department of Mechanical Engineering, City University of Hong Kong, Hong Kong 999077, China
[2]Research Center for Nature-Inspired Engineering, City University of Hong Kong, Hong Kong 999077, China
[3]Shenzhen Research Institute of City University of Hong Kong, Shenzhen 518057, China
[4]School of Chemical Engineering and Technology, Sun Yat-sen University, Zhuhai 519082, China
[5]These authors contributed equally
*Correspondence: zuanwang@cityu.edu.hk

Received: June 17, 2022; Accepted: August 8, 2022; Published Online: August 11, 2022; https://doi.org/10.1016/j.xinn.2022.100301

Citation: Song Y., Xu W., Liu Y., et al., (2022). Achieving ultra-stable and superior electricity generation by integrating transistor-like design with lubricant armor. The Innovation **3(5)**, 100301.

Extensive work have been done to harvest untapped water energy in formats of raindrops, flows, waves, and others. However, attaining stable and efficient electricity generation from these low-frequency water kinetic energies at both individual device and large-scale system level remains challenging, partially owing to the difficulty in designing a unit that possesses stable liquid and charge transfer properties, and also can be seamlessly integrated to achieve preferential collective performances without the introduction of tortuous wiring and redundant node connection with external circuit. Here, we report the design of water electricity generators featuring the combination of lubricant layer and transistor-like electrode architecture that endows enhanced electrical performances in different working environments. Such a design is scalable in manufacturing and suitable for facile integration, characterized by significant reduction in the numbers of wiring and nodes and elimination of complex interfacing problems, and represents a significant step toward large-scale, real-life applications.

INTRODUCTION

Rapid industrialization over the past decades called for new techniques to facilitate the transition from carbon-intensive fossil fuel-based energy to green, low-carbon, and renewable energy for global carbon neutrality.[1] Owing to abundance, diversity, and availability, water energy is one of the most promising green energy sources on Earth. Although the kinetic energy of water can be converted into electricity through efficient hydropower technology, a large amount of water energy in the form of raindrops, tides, and even moisture remains underused.[2–4] Their intrinsic limitations, including low frequency, sparse distribution, and variable formats impose great challenges on the efficiency, scalability, and stability of water-energy harvesting technologies.

A wide variety of new strategies based on electrokinetic,[5–8] osmotic,[9–11] triboelectric,[12–14] electromagnetic,[15–17] and piezoelectric effects[18,19] have been developed to harvest untapped water energies. In these methods, a close interplay between water and underlying interfacial materials is favored to facilitate both the mass and charge transfer. Liquid wicking in the case of electrokinetic or osmotic devices and easy liquid detachment in the case of triboelectric or piezoelectric devices can be achieved by tailoring surface wettability.[20,21] For example, droplet-based electricity generators (DE-Gs) decorated with hydrophobic or superhydrophobic surfaces demonstrate excellent dynamic water repellency and hold promise for stable and efficient energy harvesting from high-frequency water droplet effects.[22–26]

In spite of extensive efforts, the attainment of stable and efficient electricity generation at both individual device and large-scale systems levels is still difficult. First, from an individual device perspective, conventional water energy-harvesting devices are limited by low energy conversion efficiency and relatively poor durability of non-wetting surfaces in aqueous environments, especially in extreme environments (e.g., high humidity, freezing temperatures, marine environment).[22,27–31] Moreover, non-wetting surfaces are deposited with a large amount of surface charge to facilitate electricity generation and thereby absorb the counterions in water due to electrostatic attraction. The adsorbed counterions exhibit an unfavorable screening effect on the surface charges, leading to the deteriorated electrical performance of water energy-harvesting devices.[32–34] Although these challenges can be solved by the choice of lubricant layer to achieve durable interfacial materials (e.g., the slippery lubricant-infused porous surface [SLIPS]), it is limited by relatively weak electrical performance.[35,36]

Second, scaled-up integration of individual water energy-harvesting devices into systems exhibiting both excellent scalability and stability remains challenging, unlike solar energy harvesting, which can be achieved through designing integrated photovoltaic arrays. The difficulty in large-scale integration lies in designing a water energy-harvesting unit that possesses ideal liquid and charge transfer properties, and can be seamlessly integrated to achieve preferential collective performances without sacrificing the advantages inherent in individual devices. In particular, an individual device in conventional design is based on the use of separated electrode architecture characterized by the placement of two electrodes on the top and bottom of the dielectric material, which is greatly limited by the interfacing problem (convoluted wiring and redundant nodes).[37–39] For example, for a system consisting of 5 × 5 units, a total of at least 50 wires and 50 nodes are required for unit interconnection.

Here, we propose the design of a lubricant-armored transistor-like electricity generator (LA-TEG) that imparts an enhanced electrical output in a wide spectrum of harsh environments, ranging from high salinity to caustic acid-base, from low humidity to high humidity, and from low temperature to room temperature. Moreover, leveraging the conventional printed circuit board (PCB) technology, such a design reduces the number of output interfacing nodes and eliminates the complicated wire bridging, which is favorable for large-scale integration. Just like the invention of electronic transistors revolutionizing modern society, the development of the LA-TEG and its integration may provide a generic solution to large-scale and stable water energy harvesting, especially in diverse harsh environments.

RESULTS AND DISCUSSION

Design of the LA-TEG

The LA-TEG is designed to consist of a SLIPS layer, top electrode, bottom electrode, and connection circuit (Figures 1A and 1B). As shown in Figure S1, the SLIPS layer is engineered by infusing a lubricant within a superhydrophobic polytetrafluoroethylene (PTFE) membrane to transform the solid membrane into a slippery and transparent film (Figure S2 and see experimental procedures in Supplemental information), which preserves both antiwetting and easy liquid detachment.[40,41] We also delicately regulate the thickness and the viscosity of the SLIPS to achieve excellent electrical performance of LA-TEG (see Note S1 in Supplemental information). In spite of the presence of SLIPS that spatially separates the bottom electrode from the top electrode, a closed-loop circuit can be achieved for effective charge transfer and enhanced electrical output when impinging droplets bridge two electrodes.[22,42] Analogous to the electronic transistors in which the current flows from the source terminal to the drain terminal by applying voltage on the gate terminal, the impacting droplet gates the effective charge transfer between the top electrode and bottom electrode. Thus, the bottom electrode/SLIPS, the top electrode, and the water can be treated as the source, drain, and gate and called the transistor-like electrode structure, although the working principles are different.[43,44]

We chose to construct the transistor-like electrode structure and connection circuit on a PCB substrate with the aim of achieving large-scale water energy harvesting. Briefly, both the top electrode and bottom electrode are designed at the top surface of the PCB, whereas the connection circuit is constructed on the

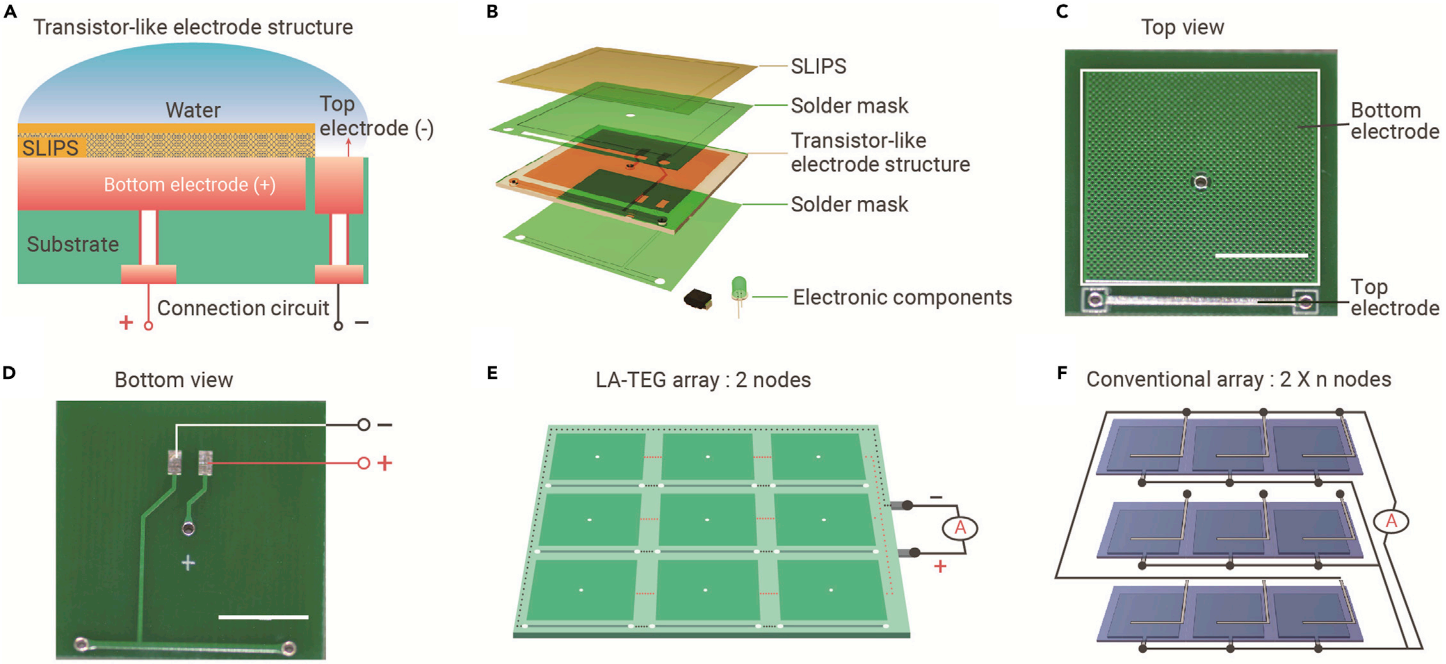

Figure 1. Design, structure, and array of LA-TEG (A) Schematic showing the transistor-like electrode design of the LA-TEG. (B) Schematic of the transistor-like electrode structure and connection circuit in single LA-TEG unit. The holes with electrodes inside are used to connect the transistor-like electrode structure and the connection circuit, which are located at the top and bottom side of the PCB, respectively. (C) Top view of a PCB substrate with the transistor-like electrode structure. Scale bar, 1 cm. (D) Bottom view of a PCB substrate in which the connection circuit is connected to the transistor-like electrode through circuits within the holes. Scale bar, 1 cm. (E and F) The construction of a 3 × 3 array of LA-TEG units requires a fewer interfacing nodes and more simplified wiring than that of the conventional array connection.

bottom surface of the PCB. Holes across the PCB are also created to fill with wires to connect two electrodes with the connection circuit (Figures 1C and 1D). Notably, the utility of the built-in connection circuit on PCB effectively mitigates the wiring problem and facilitates the integration of multiple LA-TEG units for a large-scale water energy harvester featuring variable units, fewer nodes, and built-in wiring. For example, a 3 × 3 LA-TEG array demands 2 nodes and does not need additional complicated line connections among each unit (Figure 1E). In striking contrast, for a 3 × 3 array based on conventional electrode architecture, at least 18 nodes and 18 wires are required for parallel connection with each unit (Figure 1F). Further increases in the number of units will pose severe burdens in the arrangement of nodes and wires, leading to the serious cost issue and posing a great threat to the electrical isolation of the entire system, especially in long-term contact with water.

Boosted electrical performance of LA-TEG

We measured the electrical output from LA-TEG featuring a transistor-like architecture, under the impingement of tap water of 50 μL. Briefly, under a Weber number of 80, defined as the ratio of the droplet's kinetic energy to its surface energy, a tap water droplet impinging on a single LA-TEG unit generates a peak voltage of 65 V, a current of 200 μA, and a transfer charge of 6 nC, respectively, all of which are several orders higher than those of the SLIPS-based triboelectric nanogenerator (SLIPS-TENG) (Figures 2A–2D and S3).[35,36,45–47] Such a boost in electrical performance stems from the transistor-like structure that induces an effective charge transfer (see Note S2 on the detailed circuit model analysis in Supplemental information). Before the impinging droplet contacts the top electrode, the bottom electrode possesses the same amount of electrostatically induced countercharges as that on the upper surface of SLIPS, which naturally builds a higher potential on the bottom electrode relative to the upper surface of SLIPS. In this condition, the bottom electrode and the upper surface of SLIPS serve as the bottom plate and top plate of a capacitor, respectively, constituting a capacitor C_S. When the spreading droplet connects the top electrode with SLIPS, the bottom plate (bottom electrode) and top plate (SLIPS) of the C_S are connected into a closed circuit, leading to the flow of countercharges from the bottom electrode to the top electrode. Subsequently, the droplet slides downhill and detaches from the top electrode, the circuit becomes open, and the charges flow back to the bottom electrode, ready for the electricity generation from the next falling droplet (Figure S4).

To convince the working mechanism of the transistor-like electrode structure, we further investigated the thickness of the SLIPS layer on the electrical performance of a single LA-TEG. The thickness of the SLIPS layer is responsible for the capacitance of C_S and thereby affects the output voltage of the LA-TEG according to the equation derived in our circuit model (see Note S2):

$$V = \frac{Q_S}{C_s} = \frac{Q_S d}{\epsilon S} \qquad \text{(Equation 1)}$$

where Q_s, ϵ, and S represent the stored charges, dielectric constant, and the surface area of the capacitor C_S, respectively, and d is the thickness of SLIPS layer. We find that the output voltage increases from 65 to 100 V with the increased thickness from 26 to 46 μm (Figures 2E and S5A), which is consistent with Equation (1). However, the output voltage reduces with the further increase in the thickness to 66 μm due to the reduction of the Q_s with the increased thickness of the SLIPS layer, suggesting an optimal thickness of 46 μm for the electrical performance of LA-TEG (Figure S5B).

In addition to the tap water, we substantiate that the performance improvement of LA-TEG is generic to water with various salt concentrations. Theoretically, a higher salt concentration leads to a lower electrical resistance of water and hence the internal resistance of the device.[42,48] With the thickness of SLIPS layer at 46 μm, we find that the output current increases to 1.5 mA, while the output voltage decreases to 20 V, with the increase in salt concentration from 10^{-7} to 0.6 M (Figures 2F and S6A), suggesting the mutually exclusive effect of the internal resistance on the output current and voltage. As a result, an optimized instantaneous power density of 118 $\mathrm{Wm^{-2}}$ can be obtained using a moderate salt concentration of 0.1 M rather than a higher one (Figures 2G and S6B). Such a trend is also applicable to LA-TEG, with the SLIPS thickness of 26 μm indicating the decoupling of the influence of the salt concentration of water and thickness of the SLIPS layer on the electrical performance (Figures 2H, S6C, and S6D).

Understanding the effects of the salt concentrations of water and the thickness of SLIPS enables us to achieve an optimal electrical performance of LA-TEG, such as an output voltage of 100 V, an output current of 1.5 mA, the instantaneous power density of 118 $\mathrm{Wm^{-2}}$, an average power of 0.695 mW for 1 water droplet, and an energy conversion efficiency of 0.4%. Such performances are higher than those from the previous studies involving the use of SLIPS (Figures 2I and S7).

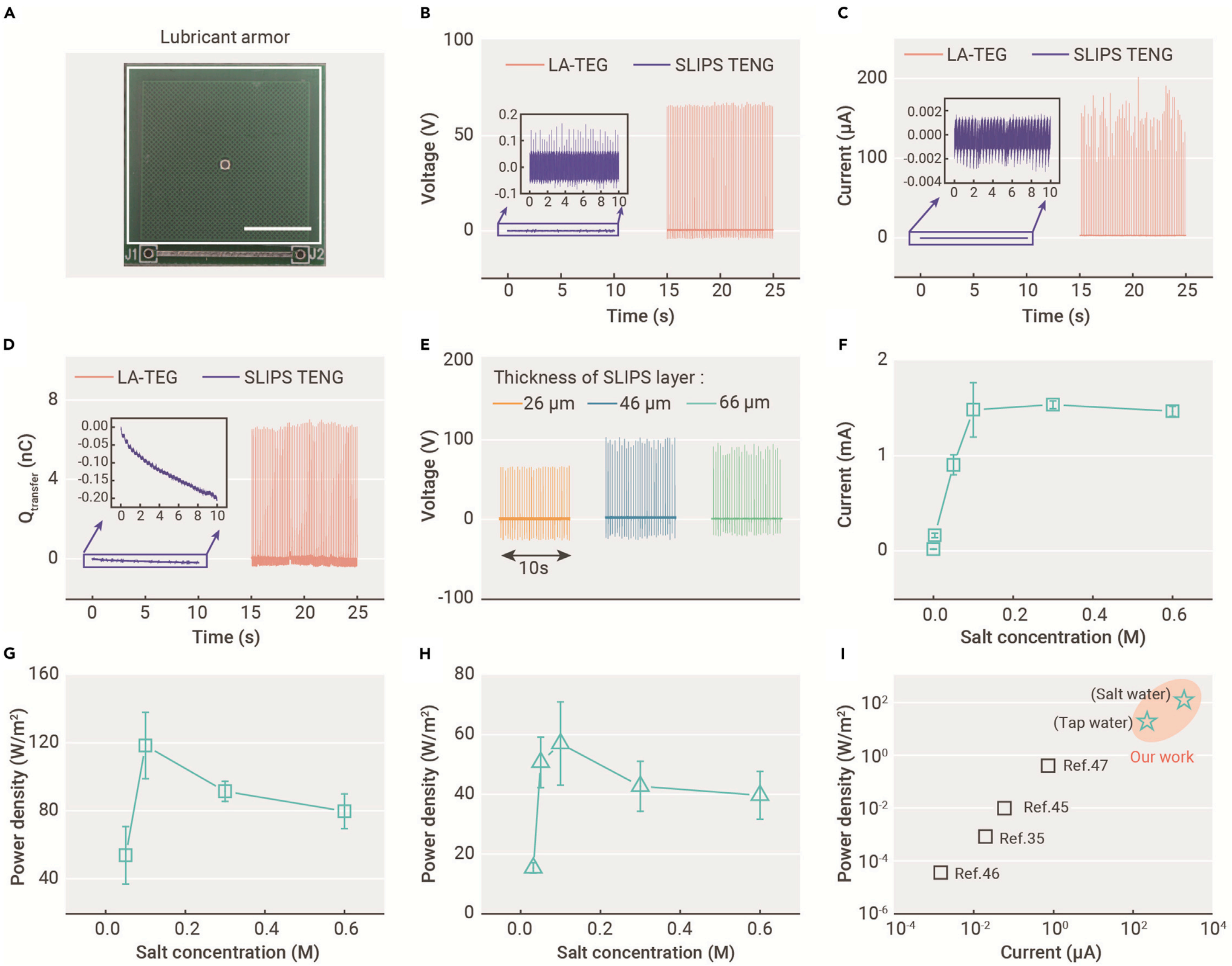

Figure 2. Electrical performance stability of LA-TEG (A) Optical image of LA-TEG consisting of PCB with transistor-like electrode architecture and SLIPS-based lubricant armor. Scale bar, 1 cm. (B–D) Under continuous tap water droplet impingement, the LA-TEG exhibits superior output voltage, current, and transfer charge than that of SLIPS TENG. The thickness of the SLIPS layer in the LA-TEG is 26 μm. (E) The output voltage of LA-TEG with varied thickness of SLIPS layer under tap water droplet impingement. (F) Increased output current of LA-TEG with the increased salt concentrations of water. The thickness of SLIPS layer is 46 μM. Data are means ± the standard error of the mean (s.e.m.). For each mean, the total number of measurements is around five. (G) The optimum instantaneous peak power density of LA-TEG with 46 μm of SLIPS layer can reach 118 Wm^{-2} when the salt concentration of the impacting droplet is 0.1 M. Data are means ± s.e.m. For each mean, the total number of measurements is five. (H) The optimum instantaneous peak power density of LA-TEG with 26 μm of SLIPS layer can reach 57 Wm^{-2} when the salt concentration of the impacting droplet is 0.1 M. Data are means ± s.e.m. For each mean, the total number of measurements is five. (I) Comparison of the peak current and instantaneous power density of this work with that of other reports involved with the lubrication coating.[35,45–47]

Very excitingly, although our previous work has shown that the salt water would cause an unfavored decay in the output voltage of devices,[22] we successfully demonstrated that the influence of the salt concentrations and the thickness of the SLIPS layer on performance can be decoupled and that carefully controlling the salt concentration and thickness can achieve higher electrical performance.

Enhanced performance stability of LA-TEG in extreme environments

The significant enhancement in the electricity generation of LA-TEG is also simultaneously achieved with enhanced stability, especially under extreme conditions, including low temperature, high humidity, and seawater. To simplify the fabrication process for the stability test, we chose LA-TEG consisting of the SLIPS layer, indium tin oxide (ITO) conductive glass, and the aluminum electrode since the electrical performance is not sensitive to the electrode materials used (Figures S8 and S9). At a freezing temperature, LA-TEG can sustain a stable output voltage beyond 50 V, 5 times higher than that of the control sample at −2°C (Figure 3A), due to the preferable anti-icing property of SLIPS than bare superhydrophobic PTFE membrane (Figure S10).[49] At high relative humidity, LA-TEG can also maintain a stable electrical output because the presence of infused lubricant timely sheds the humidity-induced condensates and prevents the formation of water film on the surface (Figures 3B and S11).[50,51] On the contrary, the control sample suffers from the rapid decay in electrical output due to the formation of a water film (Figure S12). For seawater with a high salt concentration (normal = 3.5 wt %), the voltage and current signals of LA-TEG are measured to be ~65 V and 200 μA even after 30 days of immersion, which are close to the initial electrical performance of the device (Figures 3C and S13). This result demonstrates the enhanced electrical performance stability of LA-TEG in seawater as a result of the presence of the SLIPS protection layer (Figure S14).

To illustrate the fundamental mechanisms responsible for the enhanced stability in environments of high salinity such as seawater, we examined the ion adsorption on the lubricant layer of LA-TEG. As shown in Figure S15, the lubricant layer, featuring intrinsic fluidity as well as chemical inertness, acts as a natural barrier to prevent the lodging of Na$^+$ ions attracted by the negative surface charges on PTFE, thereby ensuring the stable electrical performance of LA-TEG.[34] We further simulated ion absorption processes of LA-TEG in NaCl solution based on the molecular dynamics (MD) simulation to gain molecular-level understanding (Figure S16; Note S3 in Supplemental information). Figures 3D and 3E show the nanoscale water slab models containing Na$^+$ and Cl$^-$ ions that simulate the immersion of LA-TEG and the control in NaCl solution. As for LA-TEG, it

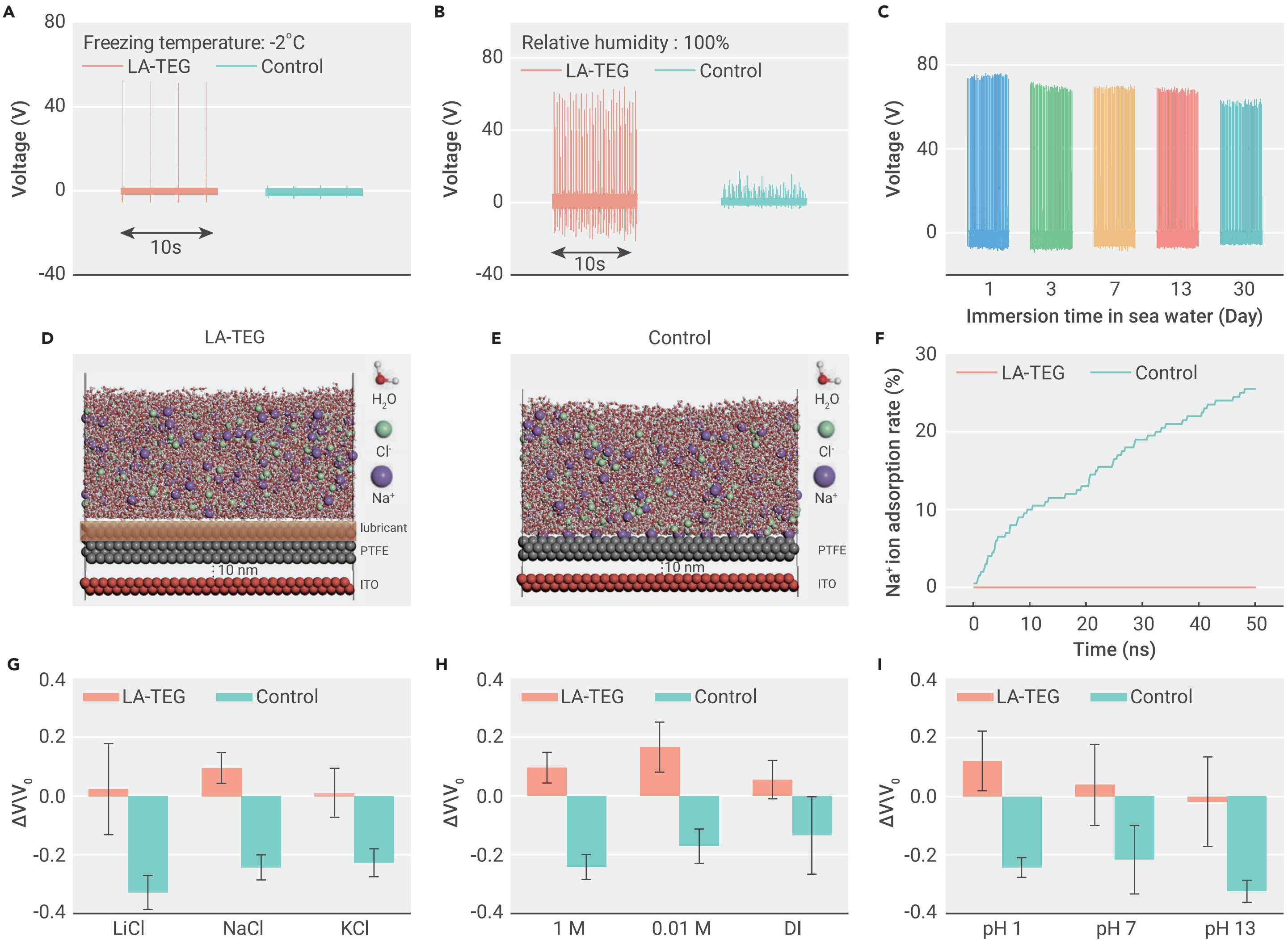

Figure 3. Principle of the stability of electrical performance of LA-TEG in ion-rich solution (A) Voltage output of an LA-TEG at −2°C for 30 min. The frequency of water droplet impingement is 0.4 Hz. (B) Voltage output of an LA-TEG at a relative humidity of 100% for 1 h. The frequency of water droplet impingement is ∼5 Hz. (C) Voltage output of an LA-TEG being immersed in seawater. (D and E) Molecular dynamics simulation showing the distribution of mobile ions (Na^+ and Cl^-) inside the water and on the LA-TEG surface as well as the control sample surface, respectively. (F) Comparison of the percentage of Na^+ being adsorbed on the LA-TEG surface and control sample surface, respectively. (G) Influence of alkali metal ions with increased atom numbers on the voltage output of a LA-TEG. Data are means ± s.e.m. For each mean, the total number of measurements is fifteen. (H) Influence of ion concentration on the voltage output of a LA-TEG. Data are means ± s.e.m. For each mean, the total number of measurements is fifteen. (I) Influence of pH value on the voltage output of a LA-TEG. Different pH values of solution are obtained by dropping 1 M HCl or NaOH into 50 mL of 1 M NaCl solutions to rule out the influence of ion concentration. Data are means ± s.e.m. For each mean, the total number of measurements is fifteen.

presents no obvious adsorption of ions on the model surface. In striking contrast, 25% of Na^+ ions in water are adsorbed on the PTFE surface of the control sample during the simulation time of 50 ns, as shown in Figure 3F. The striking contrast of ion absorption between the LA-TEG and control surface can also be verified by comparing the numbers of salt crystals on dried surfaces. As shown in Figure S17, the lubricant-infused surface is free from salt crystal coverage, while the control sample is covered by multi-sized salt crystals ranging from a few hundred nanometers to 10 μm.

The effective anti-absorption of ions rendered by lubricant armor can be further substantiated by a series of solution-immersion experiments. Figure 3G shows the voltage change ($\Delta V/V_o$) of LA-TEG immersed in solutions with different alkali ions. V_o and ΔV refer to the voltage output of the original sample before the immersion treatment and the variation of output voltage after the treatment, respectively. LA-TEG exhibits the enhanced stability of electrical performance after being soaked in solutions with Li^+, Na^+, or K^+, respectively, as evidenced by the positive voltage change rate. However, without the lubricant infusion, the control samples demonstrate the largest voltage reduction rate of −0.33 in the solution of LiCl, indicating the massive absorption of Li^+ ion on the PTFE surface, synchronous with surface charge screening. After being immersed in a solution of NaCl or KCl, the control samples show a descending voltage reduction rate of −0.24 and −0.23, suggesting the reduced absorption of Na^+ and K^+ on PTFE. We attribute these contrasting results to the lubricant armor, which can effectively prevent alkali ion absorption occurring at the PTFE surface; otherwise, PTFE tends to absorb the alkali metal ions with the smaller atom number.[7,32,52] Similar results can be found by immersing samples in solutions with increased NaCl concentrations. As shown in Figure 3H, the voltage change of LA-TEG is always positive for each concentration, while the control samples show a voltage reduction from −0.14 to −0.24, with the increasing NaCl concentration from 10^{-7} M (deionized [DI] water) to 1 M, suggesting that lubricant armor can effectively inhibit the screening effect of high salinity on surface charges. Moreover, the lubricant-induced protection sustains even in acid and base. According to Figure 3I, LA-TEG maintains a stable voltage output in the solutions of different pH, whereas the control samples suffer from the large voltage reduction of −0.25 and −0.32 in acid and base.

Practical application

LA-TEG can further be assembled into multiscale water energy harvesters that can adapt to water energy harvesting in various scenarios (Figure 4A). For instance, a LA-TEG unit constructed on a flexible PCB can serve as a condensate energy harvester that scavenges energy from water droplets that are condensed on curved walls from vapor (Figure S18). A peak voltage of up to 22 V is produced when the little condensate droplets slide across the device surface with a height difference of less than 3 cm (Figure 4B). Furthermore, we can also collect energy

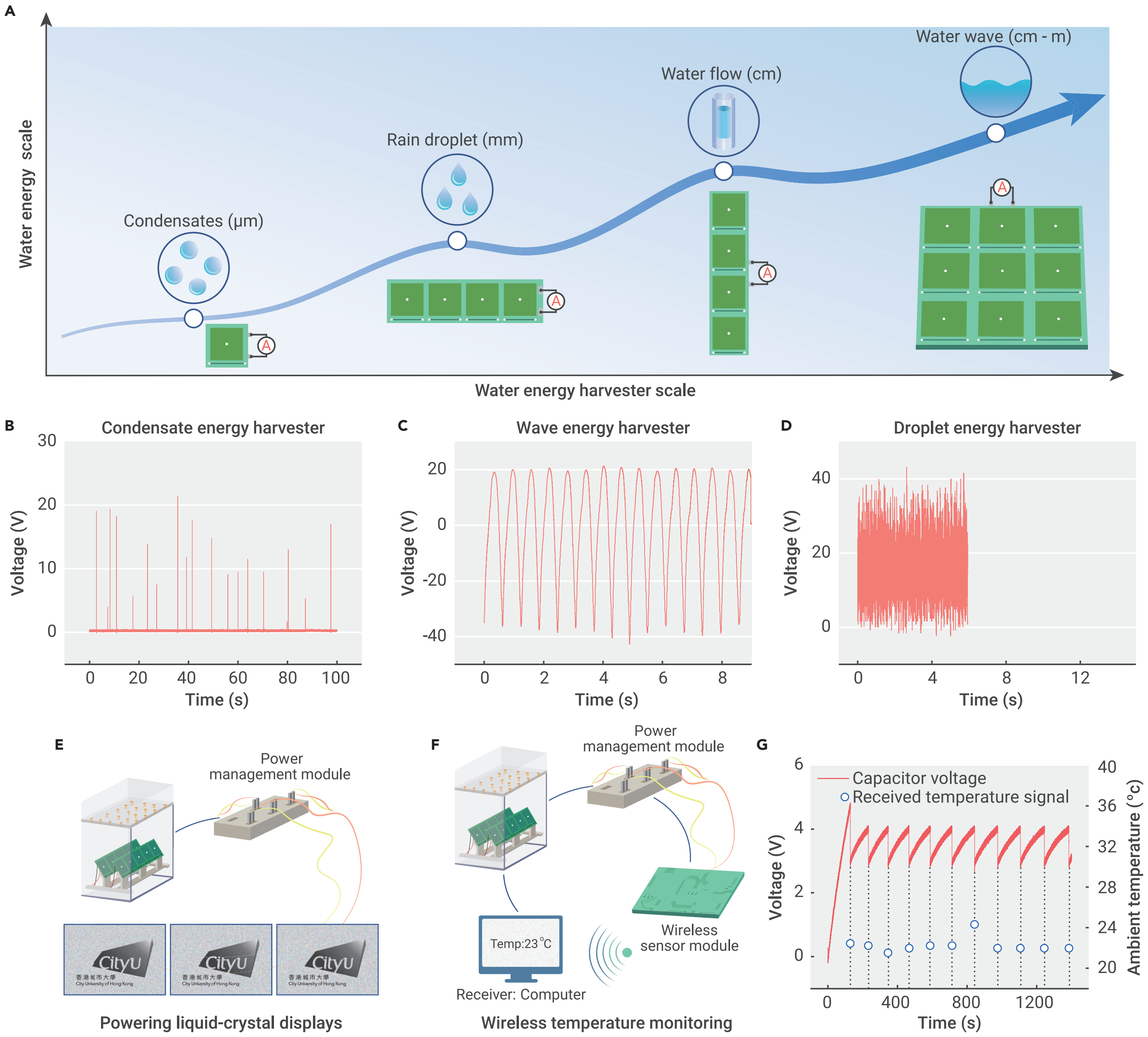

Figure 4. Application of multiscale water energy harvesters (A) Water energy harvesters, consisting of multiple LA-TEG units, are used to harvest water energy in various forms, including condensates, rain droplets, water flow, and water waves. (B) Output voltage generated by the condensate energy harvester under a vapor flow. (C) Output voltage generated by the wave energy harvester under the periodically uprising water wave. (D) Output voltage generated by the droplet energy harvester under the continuous droplet impacting. (E) Under continuous droplet impingement, the droplet energy harvester can power 3 parallel connected LCDs in real time. (F) Optical image of the wireless temperature monitoring powered by the droplet energy harvester. (G) Real-time display of the environmental temperature at every ~100 s using the wireless temperature monitoring powered by the droplet energy harvester.

from droplets by integrating horizontally arrayed LA-TEG units (Figure S19), from water flow by designing vertically arrayed LA-TEG units (Figure S20) or from water wave by the integration of horizontally and vertically arrayed LA-TEG units (Figure S21). For example, the wave energy harvester, made of 5 × 6 units, allows for electricity generation from periodical upsurges of continuous water wave and exhibits a notable peak voltage of 40 V, a current of 2 μA, and a transfer charge of 100 nC (Figures 4C and S22).

Specifically, we constructed a homemade rain droplet energy-harvesting platform by assembling five horizontally arrayed droplet energy harvesters with three-dimensional (3D)-printed droplet dispensers, as shown in Figure S23. It is worth noting that we can easily integrate the diodes into the droplet energy harvesters leveraging on our design of the built-in connection circuits on PCB substrates, aiming to overcome the offset of output signals from different LA-TEG units. Such a water energy-harvesting platform can sustain a stable output voltage up to 40 V under continuous droplet impingement (Figure 4D). As shown in Figure 4E; Video S1, the water energy-harvesting platform can successfully power three parallel connected liquid-crystal displays (LCDs) in real time. Meanwhile, combined with a power management module (Figure S24), it can also be exploited as a power supply for the wireless temperature monitoring (Figure 4F; Video S2). As shown in Figure 4G, the wireless temperature sensor can transmit the ambient temperature value to a receiver every 100 s. In this regard, our design would be a promising supplement to power sources for Internet of Things (IoT) applications in the remote and off-grid regions.[53,54]

CONCLUSIONS

In summary, we report the design of a new water harvesting device that exhibits outstanding output performance and durability, in both individual and scaled-up devices. In particular, the design can be easily integrated into the commercial connection circuit, imparting both excellent electrical performance and feasible scalability, as exemplified by the significant reduction in the amount of wiring and nodes required for device integration. In addition, the introduction of lubricant armor endows the protection of the surface charges from unwanted screening effects induced by ion absorption at the water-solid interface and ensures the stable electrical performance of LA-TEG in different harsh conditions ranging from low temperature, high humidity, and high salinity. We envision that LA-TEG would hold promise in achieving large-scale and stable water energy harvesting in diverse scenarios for applications such as wireless temperature monitoring.

REFERENCES

1. Chu, S., and Majumdar, A. (2012). Opportunities and challenges for a sustainable energy future. Nature ***488***, 294–303.
2. Lin, Z.H., Cheng, G., Lee, S., et al. (2014). Harvesting water drop energy by a sequential contact-electrification and electrostatic-induction process. Adv. Mater. ***26***, 4690–4696.
3. Scruggs, J., and Jacob, P. (2009). Harvesting ocean wave energy. Science ***323***, 1176–1178.
4. Wang, H., Sun, Y., He, T., et al. (2021). Bilayer of polyelectrolyte films for spontaneous power generation in air up to an integrated 1, 000 V output. Nat. Nanotechnol. ***16***, 811–819.
5. Zhang, Z., Li, X., Yin, J., et al. (2018). Emerging hydrovoltaic technology. Nat. Nanotechnol. ***13***, 1109–1119.
6. Xue, G., Xu, Y., Ding, T., et al. (2017). Water-evaporation-induced electricity with nanostructured carbon materials. Nat. Nanotechnol. ***12***, 317–321.
7. Yin, J., Li, X., Yu, J., et al. (2014). Generating electricity by moving a droplet of ionic liquid along graphene. Nat. Nanotechnol. ***9***, 378–383.
8. Yin, J., Zhang, Z., Li, X., et al. (2014). Waving potential in graphene. Nat. Commun. ***5***, 3582–3586.
9. Siria, A., Poncharal, P., Biance, A.-L., et al. (2013). Giant osmotic energy conversion measured in a single transmembrane boron nitride nanotube. Nature ***494***, 455–458.
10. Xin, W., Zhang, Z., Huang, X., et al. (2019). High-performance silk-based hybrid membranes employed for osmotic energy conversion. Nat. Commun. ***10***, 1–10.
11. Zhang, Z., He, L., Zhu, C., et al. (2020). Improved osmotic energy conversion in heterogeneous membrane boosted by three-dimensional hydrogel interface. Nat. Commun. ***11***, 875–878.
12. Lin, S., Chen, X., and Wang, Z.L. (2022). Contact electrification at the liquid-solid interface. Chem. Rev. ***122***, 5209–5232.
13. Wang, Y., Gao, S., Xu, W., and Wang, Z. (2020). Nanogenerators with superwetting surfaces for harvesting water/liquid energy. Adv. Funct. Mater. ***30***, 1908252.
14. Xu, W., Song, Y., Xu, R.X., and Wang, Z. (2021). Electrohydrodynamic and hydroelectric effects at the water-solid interface: from fundamentals to applications. Adv. Mater. Interfaces ***8***, 2000670.
15. Ma, Z., Ai, J., Shi, Y., et al. (2020). A superhydrophobic droplet-based magnetoelectric hybrid system to generate electricity and collect water simultaneously. Adv. Mater. ***32***, 2006839.
16. Ma, Z., Wang, Q., Wu, Z., et al. (2022). A superconducting-material-based maglev generator used for outer-space. Adv. Mater. e2203814.
17. Zhang, X., Wang, Q., Zou, R., et al. (2022). 3D-printed superhydrophobic and magnetic device that can self-powered sense a tiny droplet impact. Engineering.
18. Vatansever, D., Hadimani, R.L., Shah, T., and Siores, E. (2011). An investigation of energy harvesting from renewable sources with PVDF and PZT. Smart Mater. Struct. ***20***, 055019.
19. Xu, X., Wang, Y., Li, P., et al. (2021). A leaf-mimic rain energy harvester by liquid-solid contact electrification and piezoelectricity. Nano Energy ***90***, 106573.
20. Feng, S., Zhu, P., Zheng, H., et al. (2021). Three-dimensional capillary ratchet-induced liquid directional steering. Science ***373***, 1344–1348.
21. Liu, Y., Moevius, L., Xu, X., et al. (2014). Pancake bouncing on superhydrophobic surfaces. Nat. Phys. ***10***, 515–519.
22. Xu, W., Zheng, H., Liu, Y., et al. (2020). A droplet-based electricity generator with high instantaneous power density. Nature ***578***, 392–396.
23. Wang, L., Song, Y., Xu, W., et al. (2021). Harvesting energy from high-frequency impinging water droplets by a droplet-based electricity generator. EcoMat ***3***, e12116.
24. Wu, H., Mendel, N., van der Ham, S., et al. (2020). Charge trapping-based electricity generator (CTEG): an ultrarobust and high efficiency nanogenerator for energy harvesting from water droplets. Adv. Mater. ***32***, e2001699.
25. Helseth, L.E. (2020). A water droplet-powered sensor based on charge transfer to a flow-through front surface electrode. Nano Energy ***73***, 104809.
26. Wang, X., Fang, S., Tan, J., et al. (2021). Dynamics for droplet-based electricity generators. Nano Energy ***80***, 105558.
27. Liu, L., Shi, Q., Ho, J.S., and Lee, C. (2019). Study of thin film blue energy harvester based on triboelectric nanogenerator and seashore IoT applications. Nano Energy ***66***, 104167.
28. Tian, X., Verho, T., and Ras, R.H.A. (2016). Moving superhydrophobic surfaces toward real-world applications. Science ***352***, 142–143.
29. Varanasi, K.K., Deng, T., Smith, J.D., et al. (2010). Frost formation and ice adhesion on superhydrophobic surfaces. Appl. Phys. Lett. ***97***, 234102.
30. Amini, S., Kolle, S., Petrone, L., et al. (2017). Preventing mussel adhesion using lubricant-infused materials. Science ***357***, 668–673.
31. Sosa, M.D., Martínez Ricci, M.L., Missoni, L.L., et al. (2020). Liquid–polymer triboelectricity: chemical mechanisms in the contact electrification process. Soft Matter ***16***, 7040–7051.
32. Park, J., Yang, Y., Kwon, S.-H., and Kim, Y.S. (2015). Influences of surface and ionic properties on electricity generation of an active transducer driven by water motion. J. Phys. Chem. Lett. ***6***, 745–749.
33. Nie, J., Ren, Z., Xu, L., et al. (2020). Probing contact-electrification-induced electron and ion transfers at a liquid–solid interface. Adv. Mater. ***32***, 1905696.
34. Zhan, F., Wang, A.C., Xu, L., et al. (2020). Electron transfer as a liquid droplet contacting a polymer surface. ACS Nano ***14***, 17565–17573.
35. Xu, W., Zhou, X., Hao, C., et al. (2019). SLIPS-TENG: robust triboelectric nanogenerator with optical and charge transparency using a slippery interface. Natl. Sci. Rev. ***6***, 540–550.
36. Chung, J., Cho, H., Yong, H., et al. (2020). Versatile surface for solid–solid/liquid–solid triboelectric nanogenerator based on fluorocarbon liquid infused surfaces. Sci. Technol. Adv. Mater. ***21***, 139–146.
37. Gu, H., Zhang, N., Zhou, Z., et al. (2021). A bulk effect liquid-solid generator with 3D electrodes for wave energy harvesting. Nano Energy ***87***, 106218.
38. Chen, G., Liu, X., Li, S., et al. (2018). A droplet energy harvesting and actuation system for self-powered digital microfluidics. Lab Chip ***18***, 1026–1034.
39. Yu, J., Ma, E., and Ma, T. (2018). Exponential energy harvesting through repetitive reconfigurations of a system of capacitors. Commun. Phys. ***1***, 9–10.
40. Wong, T.-S., Kang, S.H., Tang, S.K.Y., et al. (2011). Bioinspired self-repairing slippery surfaces with pressure-stable omniphobicity. Nature ***477***, 443–447.
41. Tang, X., Li, W., and Wang, L. (2021). Furcated droplet motility on crystalline surfaces. Nat. Nanotechnol. ***16***, 1106–1112.
42. Wu, H., Mendel, N., van den Ende, D., et al. (2020). Energy harvesting from drops impacting onto charged surfaces. Phys. Rev. Lett. ***125***, 078301.
43. Yang, Z.W., Pang, Y., Zhang, L., et al. (2016). Tribotronic transistor array as an active tactile sensing system. ACS Nano ***10***, 10912–10920.
44. Wu, H., Wang, S., Wang, Z., and Zi, Y. (2021). Achieving ultrahigh instantaneous power density of 10 MW/m2 by leveraging the opposite-charge-enhanced transistor-like triboelectric nanogenerator (OCT-TENG). Nat. Commun. ***12***, 5470–5478.
45. Nie, J., Wang, Z., Ren, Z., et al. (2019). Power generation from the interaction of a liquid droplet and a liquid membrane. Nat. Commun. ***10***, 2264.
46. Wang, P., Zhang, S., Zhang, L., et al. (2020). Non-contact and liquid–liquid interfacing triboelectric nanogenerator for self-powered water/liquid level sensing. Nano Energy ***72***, 104703.
47. Wu, J., Xi, Y., and Shi, Y. (2020). Toward wear-resistive, highly durable and high performance triboelectric nanogenerator through interface liquid lubrication. Nano Energy ***72***, 104659.
48. Li, X., Ning, X., Li, L., et al. (2022). Performance and power management of droplets-based electricity generators. Nano Energy ***92***, 106705.
49. Kim, P., Wong, T.-S., Alvarenga, J., et al. (2012). Liquid-infused nanostructured surfaces with extreme anti-ice and anti-frost performance. ACS Nano ***6***, 6569–6577.
50. Hao, C., Li, J., Liu, Y., et al. (2015). Superhydrophobic-like tunable droplet bouncing on slippery liquid interfaces. Nat. Commun. ***6***, 7986–7987.
51. Smith, J.D., Dhiman, R., Anand, S., et al. (2013). Droplet mobility on lubricant-impregnated surfaces. Soft Matter ***9***, 1772–1780.
52. Park, J., Song, S., Shin, C., et al. (2018). Ion specificity on electric energy generated by flowing water droplets. Angew. Chem. Int. Ed. Engl. ***57***, 2091–2095.
53. Xi, F., Pang, Y., Liu, G., et al. (2019). Self-powered intelligent buoy system by water wave energy for sustainable and autonomous wireless sensing and data transmission. Nano Energy ***61***, 1–9.
54. Ahmed, A., Saadatnia, Z., Hassan, I., et al. (2017). Self-powered wireless sensor node enabled by a duck-shaped triboelectric nanogenerator for harvesting water wave energy. Adv. Energy Mater. ***7***, 1601705.

ACKNOWLEDGMENTS

We acknowledge the financial support of the Research Grants Council of Hong Kong (nos. C1006-20WF and 11213320), the Tencent Foundation through the XPLORER PRIZE, the Innovation and Technology Council (no. 9440248), the National Natural Science Foundation of China (grant nos. 51975502 and 21621001), and the 111 Project (B17020). We also thank Mr. Pan Zhenghua for his contribution to the design and manufacture of the PCB substrate.

AUTHOR CONTRIBUTIONS

Z.W. conceived and supervised the research. Y.S. and W.X. designed the experiments. H.Z., M.C., and Y.Z. participated in the discussion of the experimental design. Y.S., B.Z., and L.W. prepared and characterized the samples. Y.S., W.X., and H.Z. constructed the experimental platform. X.Y., X.X., P.L., and Z.Y. conducted the construction of the wireless temperature monitoring. Y.S. assembled and characterized the samples and carried out the experiments. Y.S., W.X., and Y.L. discussed the models. Y.L. built the MD models. All of the authors analyzed the data. Z.W. wrote the manuscript, with the input of all of the other authors.

DECLARATION OF INTERESTS

The authors declare no competing interests.

SUPPLEMENTAL INFORMATION

Supplemental information can be found online at https://doi.org/10.1016/j.xinn.2022.100301.

The Innovation, Volume *3*

Supplemental Information

Achieving ultra-stable and superior electricity generation by integrating transistor-like design with lubricant armor

Yuxin Song, Wanghuai Xu, Yuan Liu, Huanxi Zheng, Miaomiao Cui, Yongsen Zhou, Baoping Zhang, Xiantong Yan, Lili Wang, Pengyu Li, Xiaote Xu, Zhengbao Yang, and Zuankai Wang

Supplemental Data Items

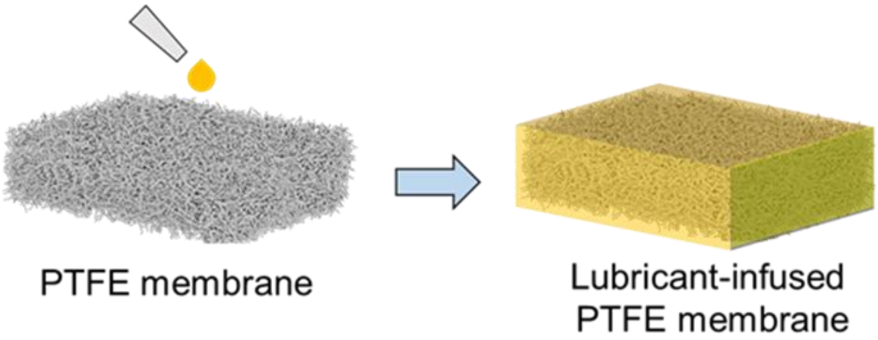

Figure S1. Schematics showing the fabrication of the SLIPS layer.

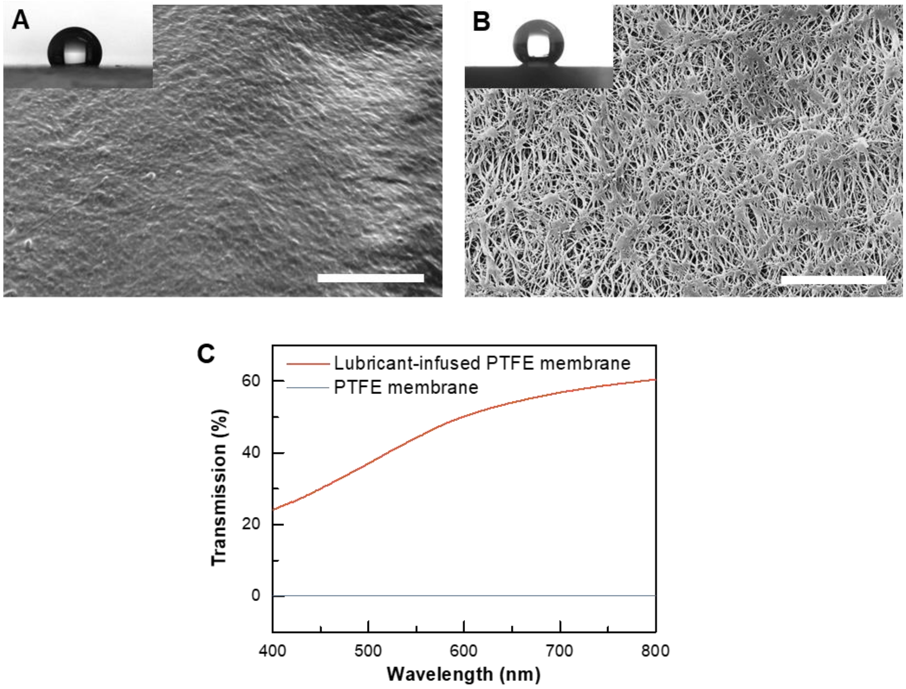

Figure S2. Structure, wettability and optical characterization of SLIPS and PTFE membrane.

(A) SEM image (top view) of SLIPS shows smooth and liquid-like morphology. Inset image measures a static contact angle of 124.4° ± 1.72°. (Scale bar, 30 μm)

(B) SEM image (top view) of PTFE membrane shows nano-porous morphology. Inset image measures a static contact angle of 153.9° ± 3.11° (Scale bar, 10 μm).

(C) Optical transmittance of SLIPS and PTFE membrane.

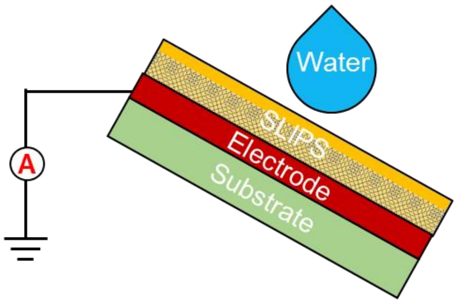

Figure S3. The structure of SLIPS TENG consisting of a SLIPS layer and a single electrode.

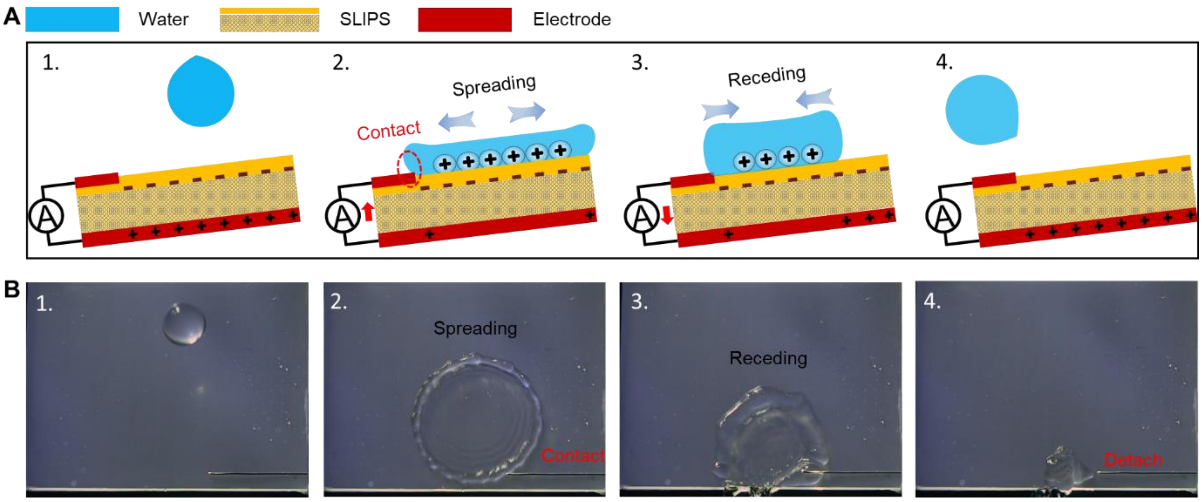

Figure S4. Schematics and snapshots of electricity generation in LA-TEG.

(A) 1. Before a droplet contacts the SLIPS in LA-TEG, all countercharges induced by the surface charges on SLIPS locates at the bottom electrode, resulting in a great potential difference across the SLIPS layer. 2. Once a droplet spreads and bridges the top electrode and SLIPS into a closed-circuit, the electrostatically induced higher potential on bottom electrode as opposed to the SLIPS leads to the building of an electric field, driving the flow of countercharges from the bottom electrode to the top electrode to generate the electricity output. Meanwhile, counter-charged ions in water are driven to screen the surface charge of SLIPS. 3. Then the droplet begins receding and the contact area between water and SLIPS is reduced, resulting in the flow of countercharges back to bottom electrode. 4. When the droplet slides downhill and detaches from top electrode, the circuit becomes open and all charges flow back to the bottom electrode, ready for the electricity generation from next falling droplet.

(B) Snapshots of dynamic droplet impacting process on LA-TEG corresponding to the electricity generation process.

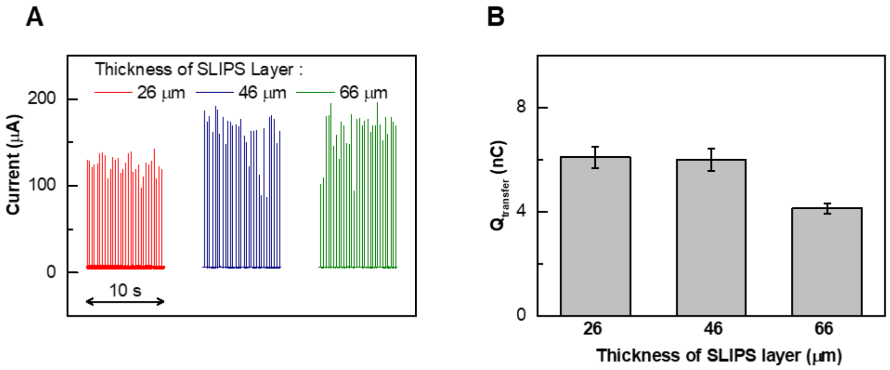

Figure S5. Electrical performance of LA-TEG with the varied thickness of SLIPS layer. (A-B) Output voltage and transfer charge of LA-TEG with the varied thickness of SLIPS layer ranging for 26 μm to 66 μm. (Tap water droplet volume of 50 μL and release height of 12 cm)

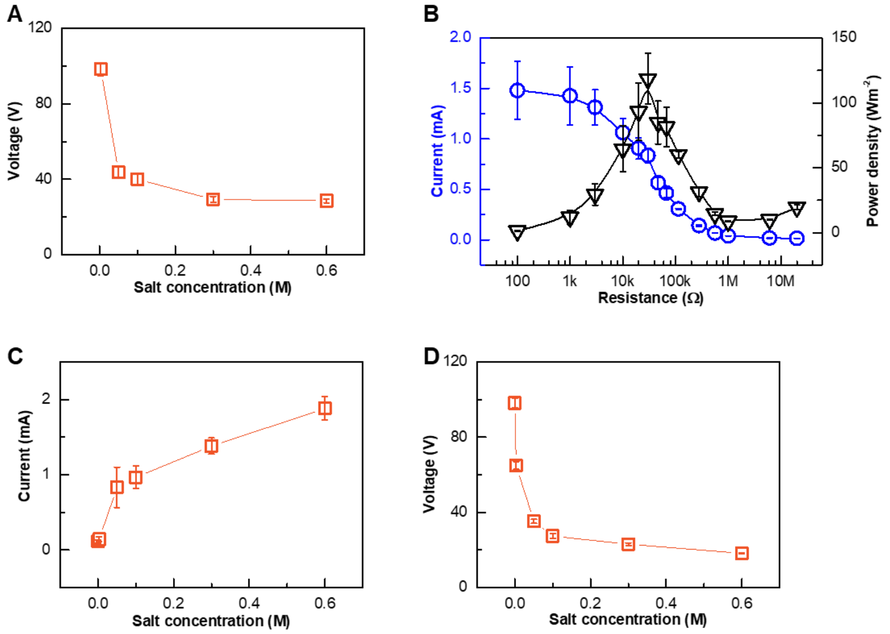

Figure S6. Electrical performance of LA-TEG under continuous impingement of saltwater droplets.

(A) The output voltage of LA-TEG with SLIPS thickness of 46 µm under varied salt concentrations.

(B) Instantaneous power density of the LA-TEG under 0.1M Nacl solution as a function of loading resistance. (SLIPS layer of 46 µm, water droplet volume of 50 µL, release height of 12 cm)

(C) Increased output current of LA-TEG with the increased salt concentrations of water. The thickness of SLIPS layer is 26 µm

(D) The output voltage of LA-TEG with SLIPS thickness of 26 µm under varied salt concentrations.

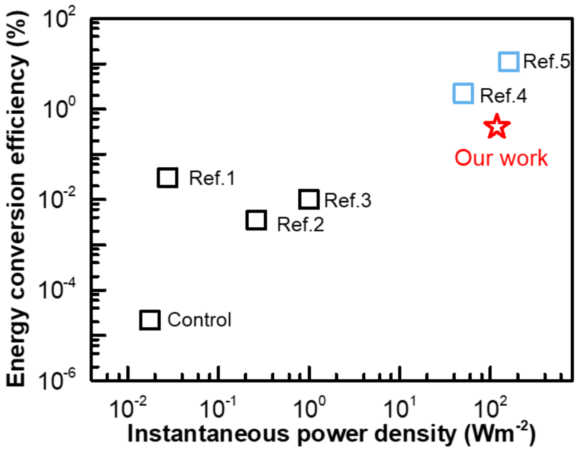

Figure S7. The energy conversion efficiency of our work and some previous work. Our work, TENGs[1-3] and other DEGs[4,5] are represented in red, blue and black, respectively. We demonstrate that our work shows the most stable energy conversion efficiency of 0.4% in spite of the relative low value compared to the generator without the use of SLIPS. Such a stable energy conversion efficiency endowed by the SLIPS facilitates the further practical applications of our design.

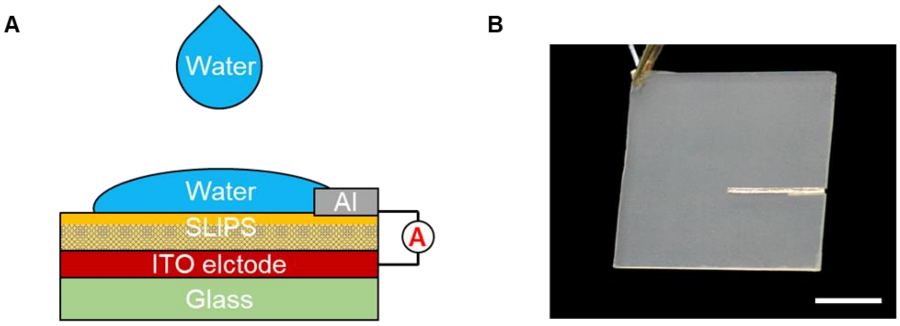

Figure S8. LA-TEG prepared for the stability test.

(A) The LA-TEG consisting of the SLIPS layer, ITO conductive glass and aluminum electrode.

(B) Optical image of the ITO-based LA-TEG.

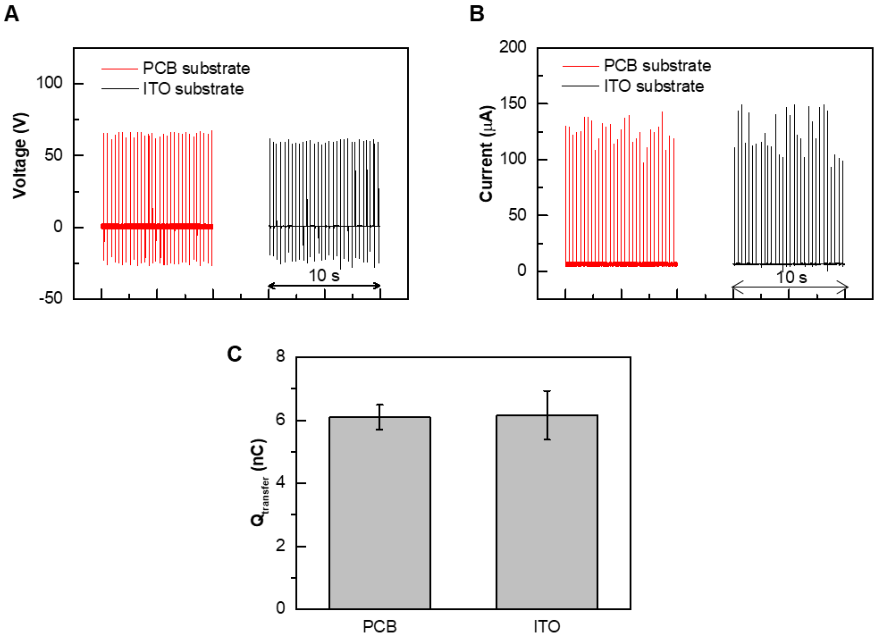

Figure S9. The output voltage, current and transfer charge of the PCB-based and ITO-based LA-TEGs without the extra charging treatment.

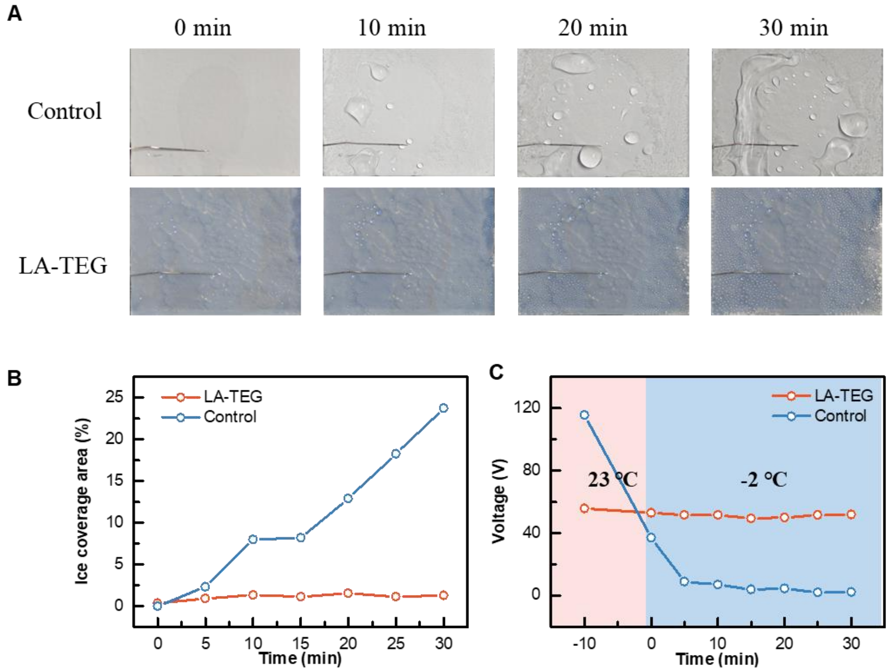

Figure S10. The electrical performance stability of the LA-TEG in the freezing temperature.

(A) Snapshots of icing process on surfaces of LA-TEG and the control sample at -2 ℃. No ice was observed on the LA-TEG while the ice coverage area gradually increased on control surface over time because the lubricant layer can effectively delay ice/frost formation and enhance droplet mobility.

(B) Ice coverage ratio of LA-TEG and control sample at -2 ℃.

(C) Time variation of the LA-TEG’s output voltage signal at -2 ℃.

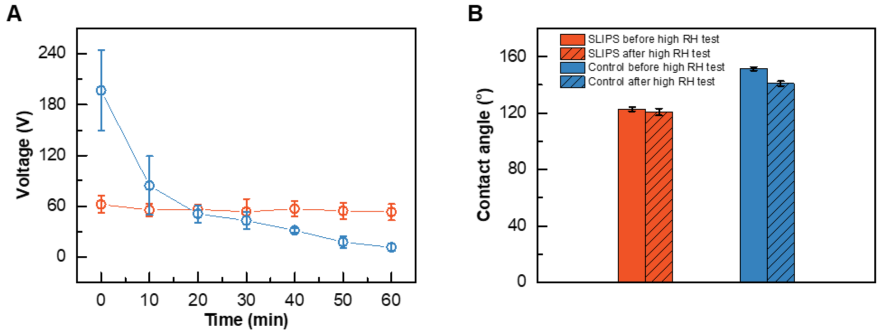

Figure S11. The electrical performance stability of the LA-TEG in the highly humid environment.

(A) Time variation of the LA-TEG’s output voltage signal at relative humidity of 100%.

(B) The contact angles of LA-TEG before and after the high humidity test.

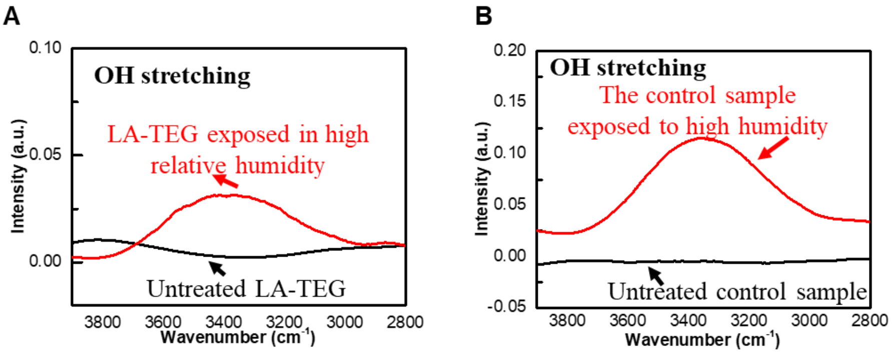

Figure S12. FTIR spectra of the LA-TEG and control sample surfaces prepared under different conditions. Dried samples (black curves) were previously stored under dry conditions. The red curves correspond to test samples that were previously exposed to water vapor. The FTIR spectra of the control sample without the use of lubricant exhibit more strong bands at ca. 3500 cm^{-1}, which is assigned to the stretching vibrational modes of water, suggesting that more water is absorbed on the surface of the control sample than that of LA-TEG.

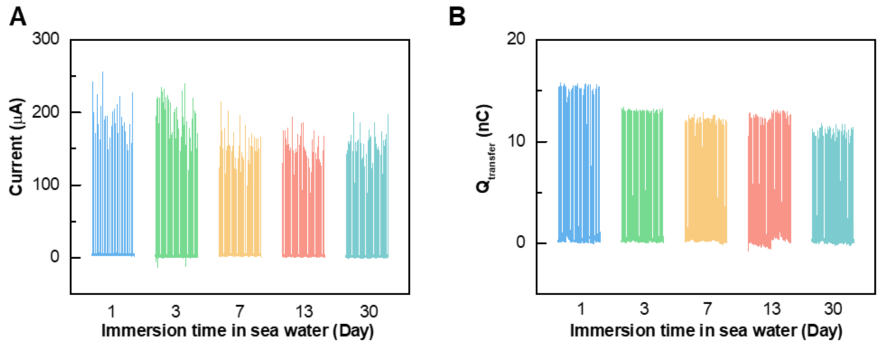

Figure S13. Electrical performance of LA-TEG after the immersion treatment in seawater for 30 days.

(A and B) The time-dependent variation of output current and transfer charge of LA-TEG. The LA-TEG was precharged with a large charge density before the test.

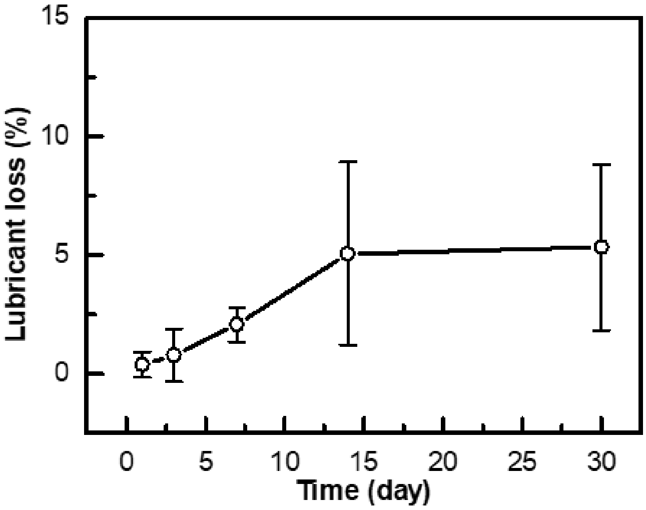

Figure S14. The lubricant loss in LA-TEG when immersed in seawater. There is only 5% loss in the lubricant mass after immersion treatment for 30 days, indicating a long-term durability of the lubricant layer in seawater

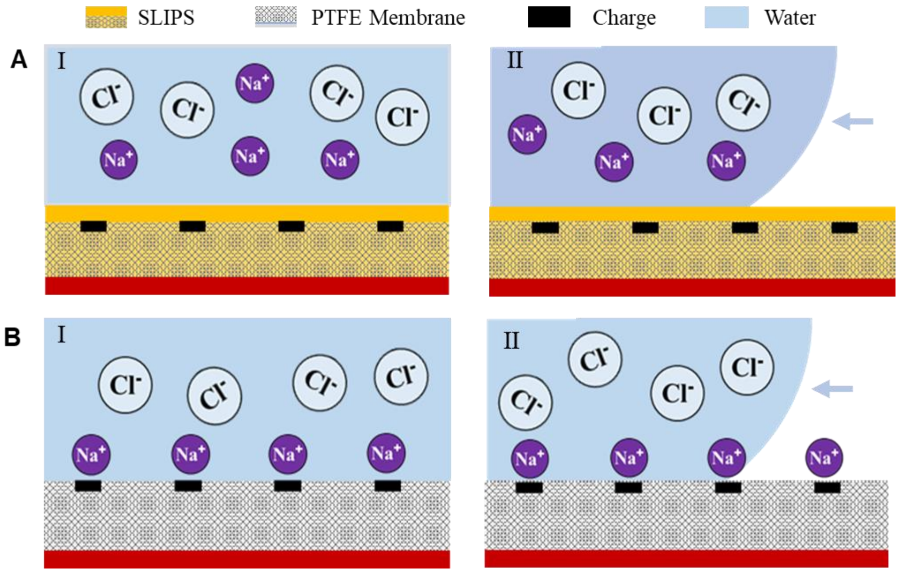

Figure S15. Schematics showing the prevention of ion absorption on LA-TEG using a SLIPS layer.

(A) When LA-TEG is immersed into the solution, the lubricant layer acts as a natural barrier and prevents the lodging of those ions attracted by the negative surface charge on SLIPS. Simultaneously, the lubricant can also mitigate the counter-ion absorption due to its intrinsic fluidity as well as chemical inertia.

(B) Without the use of the lubricant armor, the ions in water can be firmly absorbed onto the PTFE surface of the control sample due to the strong electrostatic attraction between the negative surface charges and the counterions. These adsorbed counterions still remain stationary on the PTFE surface even when the solution is completely detached, which thereby screen the surface charges on PTFE.

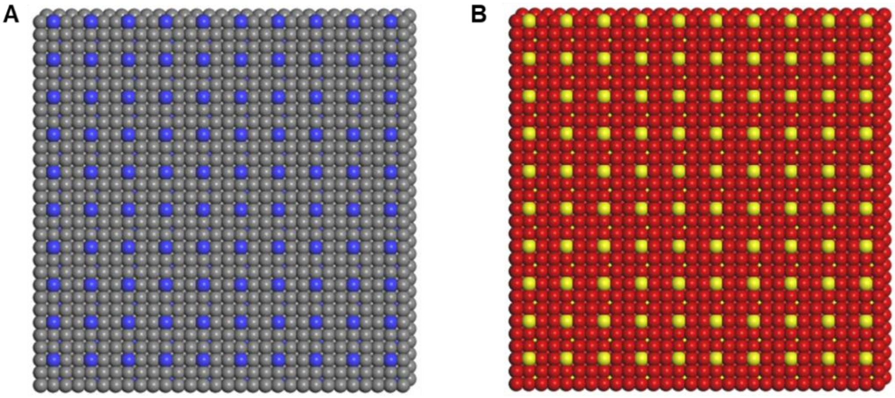

Figure S16. Charge distribution on PTFE and ITO in the models of the systems employed in the Molecular Dynamic (MD) simulations.

(A) 100 negative charges (blue) with decent space are set on the first layer of PTFE (grey).

(B) 100 positive charges (yellow) are fixed on the ITO electrode (red).

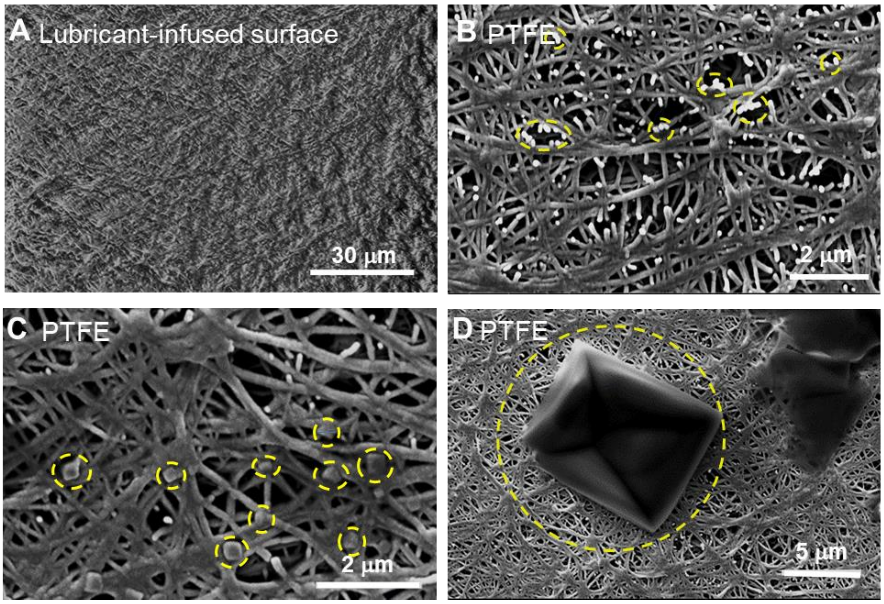

Figure S17. Characterization of salt crystals formed on SLIPS and PTFE surface after immersion in 0.6M NaCl solution for 6 hours.

(A) No salt crystal was observed on the smooth and liquid-like SLIPS.

(B-D) Salt crystals with different sizes ranging from tens nanometers to several micrometers were found on PTFE membrane.

Figure S18. Optical image showing condensed droplets sliding over the condensate energy harvester attached to a curved surface. The condensate energy harvester is made of a SLIPS layer and a flexible printed circuit board integrated with transistor-like electrode architecture.

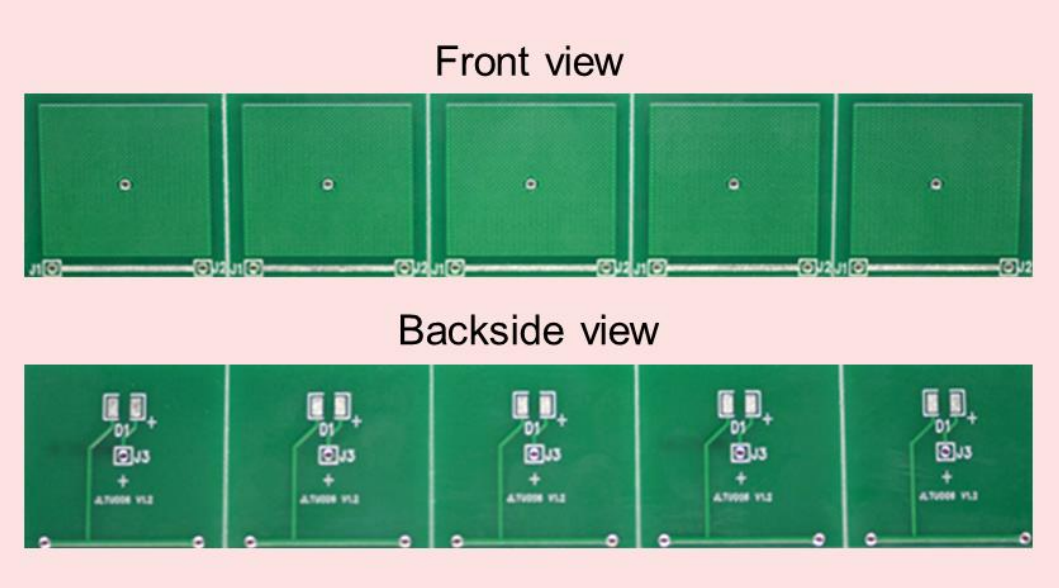

Figure S19. Optical images of the droplet energy harvester consisting of 5 pieces of LA-TEGs.

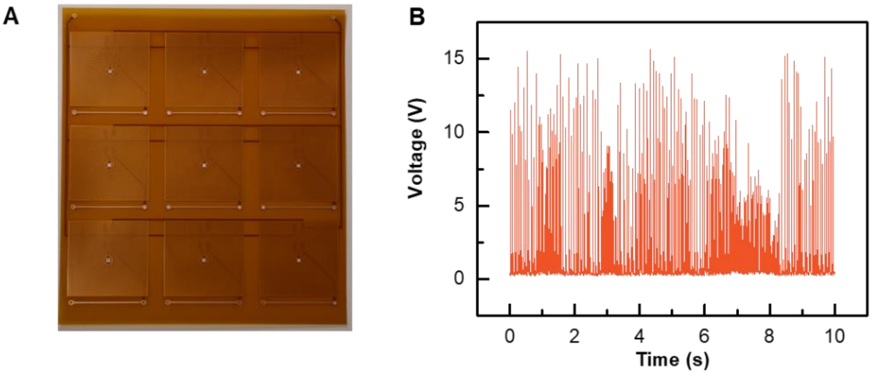

Figure S20. Flow energy harvester.

(A) Optical images of the flow energy harvester consisting of 3×3 pieces of LA-TEGs made by flexible printed circuit boards.

(B) The output voltage of the flow energy harvester under intermittent water flow.

Figure S21. Optical images of the wave energy harvester consisting of 6×5 pieces of LA-TEGs.

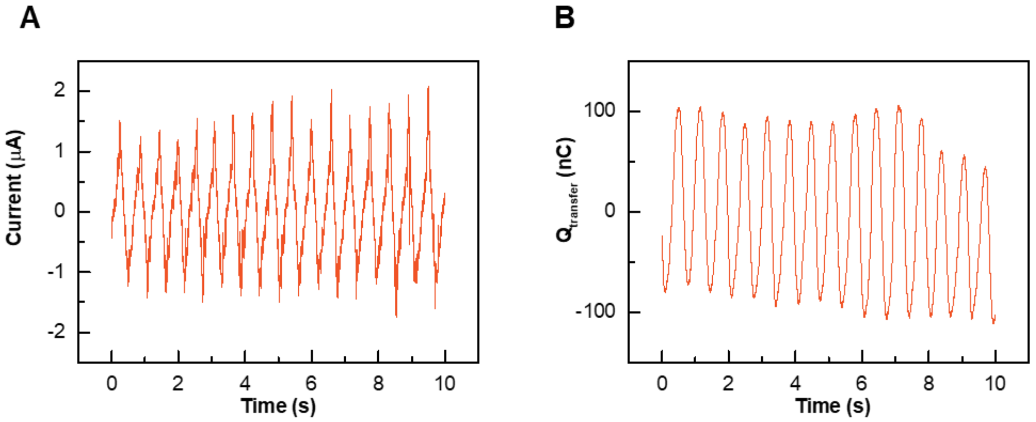

Figure S22. Output current and transfer charge of a wave energy harvester under periodically uprising waves.

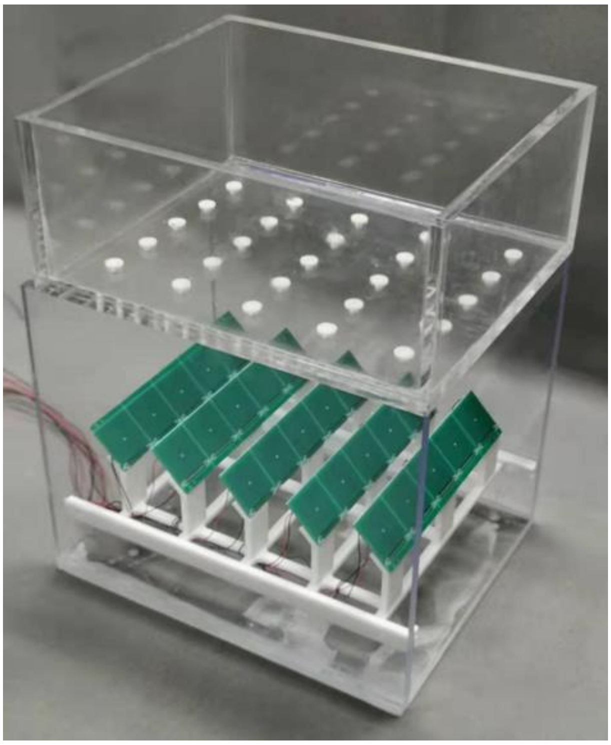

Figure S23. A home-made rain-droplet energy harvest platform is composed of five pieces of droplet energy harvesters, 3D-printed dispensers and sample supports.

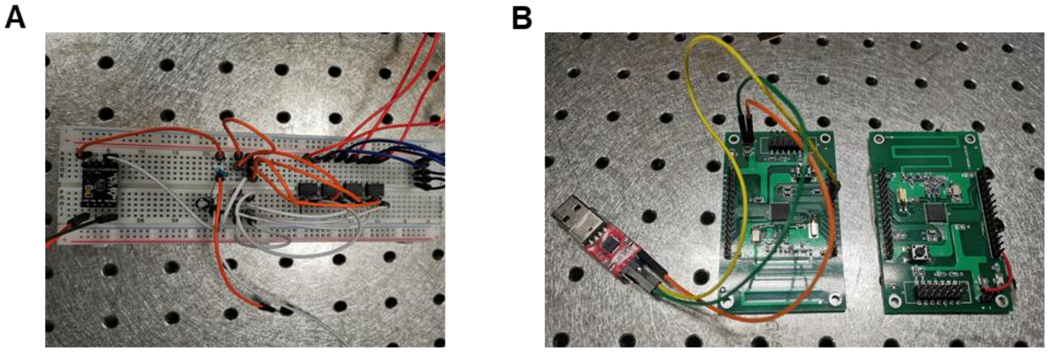

Power management module

Wireless sensor module

Figure S24. Power management module and wireless temperature sensor module.

(A) The power management module consists of a bridge circuit, a capacitor of 25 μF, and a nanopower energy harvesting power supply (GY-LTC3588).

(B) The wireless temperature sensor module consists of a set of wireless development board (CC430F5137) and a serial to USB adaptor for transmitting signal to the computer.

Note S1

Regulation of lubricant layer thickness and lubricant type

We controlled the thickness of lubricant layer h by the control of volume of lubricant V according to the equation $h = (V\text{-}V_{pore})/A=(V\text{-}kV_{PTFE})/A$, where A is the area of PTFE membrane and V_{pore} is the volume of lubricant trapped in the pores of the PTFE membrane, which is related to the volume of the PTFE membrane (V_{PTFE}) and the porosity of the membrane (k). As shown in the figure below, the output voltage of LA-TEG gets decreased as the lubricant layer thickness is beyond 7 μm. This is because the thicker lubricant layer will hinder the electrical interaction between the charge carriers in water droplets and surface charge accumulated on the PTFE surface, thus resulting in the inefficient utilization of surface charge for electricity generation. In this regard, we fixed the lubricant layer thickness of LA-TEG as 6 μm in all experiments.

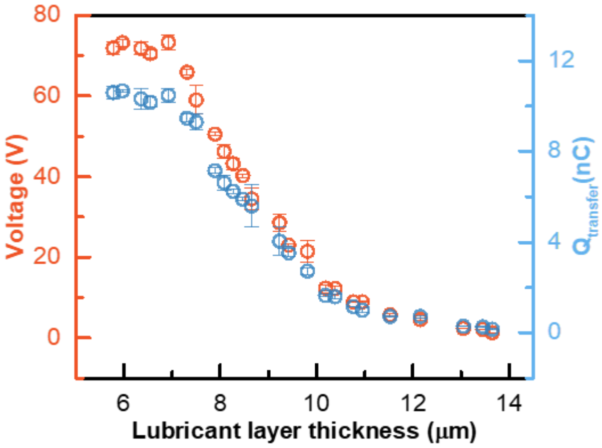

Output voltage and transfer charge as a function of lubricant layer thickness of SLIPS in LA-TEG.

We also investigate the effect of lubricant type on the electrical performance of LA-TEG. As shown in the figure below, Krytox 103 and105 endow LA-TEG with the best performance due to their proper viscosity and relative permittivity. In this regard, Krytox 103 is used in all experiments in this paper owing to its smaller viscosity than Krytox 105.

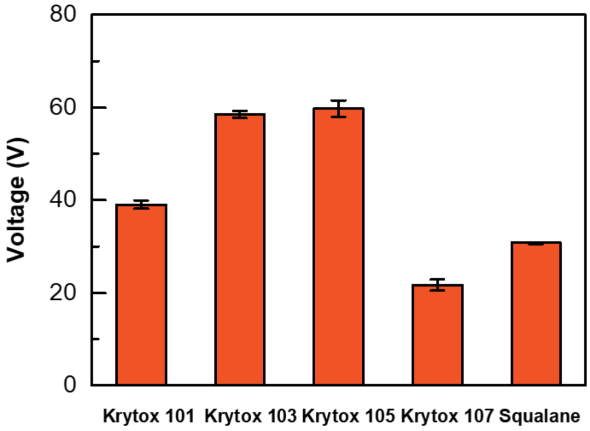

Output voltage of LA-TEG with varied infused lubricants

Note S2

Circuit analysis of LA-TEG.

The dramatic boost of electrical performance of LA-TEG is attributed to the transistor-like design. Since the influence of the charge of droplet itself and dropper can be ruled out, we can shed light on the working mechanism of LA-TEG based on the equivalent circuit analysis. As plotted in the below Figure A, when a water droplet impacts on the surface, LA-TEG can be treated as three serially connected capacitors C_s, C_1 and C_2, respectively. Among them, the capacitor C_s consists of the SLIPS layer (dielectric), SLIPS surface (upper plate), and electrode (bottom plate). The two electric double layer (EDL) capacitors, C_1 and C_2, are formed at the water/SLIPS interface as well as the water/electrode interface, respectively. Water itself can be treated as a resistor in this circuit. In this regard, prior to the contact between water droplet and electrode to form C_2 for charge transportation, the circuit is on an open state without charge transfer. Once the water droplet contacts the electrode, the instant formation of C_2 connect the originally disconnected system to a closed circuit. Therefore, under the giant electric potential induced by the high-density surface charge stored in SLIPS, plenty of charges are forced to transfer in the circuit (Figure B), resulting in an instantaneous peak voltage signal. The equivalent circuit is shown in Figure A, governed by the following differential equation:

$$(R_l + R_w)\frac{dq(t)}{dt} = \frac{Q_S - q(t)}{C_S} - \frac{q(t)}{C_1(t)} - \frac{q(t)}{C_2(t)} \tag{1}$$

$$q(t = 0) = 0 \tag{2}$$

where $q(t)$ is the transfer charge, and R_L and R_w are the impedance of the external load and water, respectively. As the thickness of EDL is far smaller than the thickness of SLIPS, $C_s \gg C_1,\ C_2$. Thus, equation (1) can be expressed as:

$$(R_l + R_w)I = \frac{Q_S}{C_S} = V \tag{3}$$

where I is the output current and V is the output voltage of LA-TEG, respectively. In this regard, with a fixed Q_s and C_s, reducing the resistance of water can achieve an improved output current. Introducing the capacitor equation, the output V is governed by the following equation:

$$V = \frac{Q_S}{C_S} = \frac{Q_S d}{\varepsilon S} \tag{4}$$

where d, ε and S represent the thickness, dielectric constant and the surface area of the capacitor C_s. We can conclude that output voltage increases linearly with the SLIPS thickness if Q_s is constant.

Our analysis can be further validated through the careful synchronization of the droplet spreading dynamic as well as the time-dependent evolution of the output voltage (Figure C and D). When the water droplet contacts the LA-TEG, the system is in a switch-off state and there is no electrical output signal. Then the droplet spreads out and contacts the electrode, transforming the system into a switching-on state. At this critical time t_{on} = 0 s marking the timepoint of water-electrode contact, a pronounced voltage signal emerges with rapid flow of charges from ITO to the electrode. At t_{off} = 0.025 s, the water droplet detaches from the electrode accompanied with the reduction of the voltage signal to zero, indicating that the transferred charges move back to the ITO. Careful inspection of the droplet spreading dynamic on SLIPS shows the contact time of the droplet and electrode is about 25 ms which closely corresponds to the voltage signal duration time $t_{off} - t_{on}$.

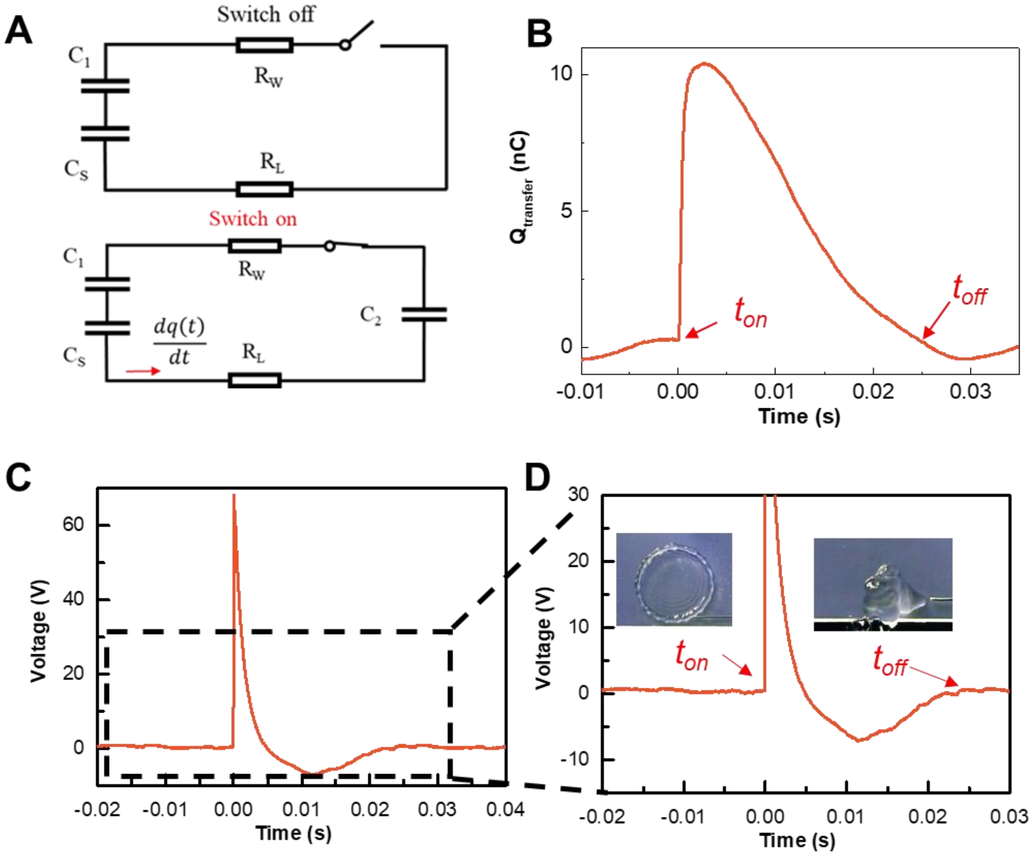

Circuit model and synchronization of droplet-spreading dynamics and voltage response. (A) In the switched-off mode, there is no capacitor formed at the water/top electrode interface because the water droplet has not approached the electrode. As a result, the capacitors C_S and

C_1 remain in an open circuit and there is no charge flow between them. b, Once the water droplet contacts the electrode, the instant formation of capacitor C_2 connect the originally disconnected system to a closed circuit. R_w, R_L and $dq(t)/dt$ in the circuit are, respectively, the impedance of the water droplet, the impedance of the external load and the derivative of the transferred charge with respect to time.

(B) Time-dependent variation in the transferred charge, $Q_{transfer}$, generated on the ITO-based LA-TEG by an impinging droplet, indicating that the process of charge transfer corresponds to the change of the equivalent circuit from switch-on state to switch-off state. The ITO-based LA-TEG was precharged with a large charge density before the test.

(C and D) Synchronization of droplet-spreading dynamics and voltage response of ITO-based LA-TEG. Insets are snapshots showing the snapshots of the droplet dynamics. The ITO-based LA-TEG was precharged with a large charge density before the test.

Note S3

Molecular dynamics simulations.

To investigate the effect of immersion in aqueous solution, we carried out molecular dynamics (MD) simulations. Nanoscale slab models containing about 1.0×104 water molecules with 200 sodium and 200 chlorine ions were employed to simulate the behavior of ions during the immersion processes (Figure S15). To mimic the charged PTFE, rigid atomic layers were used, and negative charges were fixed on the first and second atomic layers with a spacing of 8.7 Å, and equivalent positive charges were fixed on the atomic layers of ITO electrode; each site was charged +e or –e. For the SLIPS case, three more atomic layers were used to represent the lubricant. The box size of the systems was 8.7 nm × 8.7 nm × 30.1 nm, in which the thickness of the aqueous solution was about 4.5 nm. Periodic boundary conditions were applied in the x and y directions. The intermolecular interactions among water molecules were described by using TIP4P/ICE potential. The parameters of Na+ and Cl- are σNa=2.876 Å, εNa=0.5216 kJ/mol, σCl=3.785 Å, εCl=0.5216 kJ/mol as reported in previous work. The cross Lennard-Jones interaction parameters between water and sodium and chlorine ions were obtained based on Lorentz-Berthelot rule. The interactions between substrate atoms (sub) and NaCl water solution were described in the form of 12-6 Lennard-Jones potential with parameters of $\sigma Na\text{-}sub$=3.021 Å, $\varepsilon Na\text{-}sub$=0.4785 kJ/mol, $\sigma Cl\text{-}sub$=3.476 Å, $\varepsilon Cl\text{-}sub$=0.4785 kJ/mol, and $\sigma O\text{-}sub$=3.458 Å, $\varepsilon O\text{-}sub$=0.6223 kJ/mol. Leap-frog algorithm was selected for the integration of newton's equations of motion in the MD simulations with a time step of 1 fs. Fast smooth particle-mesh Ewald method was used for electrostatic interactions with a real-space cutoff 10 Å. The van der Waals interactions were truncated at 10 Å. Nosé-Hoover scheme was employed to control the system temperature at 300 K. All the MD simulations were carried out by using Gromacs 4.5.5 software. First, the aqueous solution with Na^+ and Cl^- were running to reach equilibrium at 300 K without any charges fixed on the substrates. Next, we performed constant-temperature and constant-volume (NVT) MD simulations of the immersion processes for both Control and SLIPS in the time of 50 ns.

Experimental Procedures

Materials.

Hydrochloric acid, Sodium hydroxide, Sodium chloride, Potassium Chloride, Lithium Chloride, Acetone (RCI Labscan, 99,5%), ethanol (Sigma Aldrich, 97%), deionized water, seawater (obtained from Victoria Harbour, Hong Kong), Krytox perfluoropolyether oils (Chemours, GPL 101, 103, 105, 107), and Squalene (J&K Scientific Ltd., 97%) were used without further purification. The dimension of purchased Indium Tin Oxide (ITO) glass (Huananxiangcheng Technology Ltd.) are 3.0 cm×3.0 cm×1.0 mm. The thickness and average pore size of porous PTFE membrane (Sterlitech Corporation, PTU023001) are 20 μm and 200 nm, respectively. PCB substrates with the transistor-like electrode structure were provided by a commercial company.

Fabrication of the LA-TEG.

To fabricate the LA-TEG, a PCB substrate was first ultrasonically cleaned in ethanol for 10 min. Then we gently covered a porous PTFE membrane onto the PCB substrate. To ensure a good contact between the PTFE membrane and PCB substrate, the membrane was first wetted by ethanol with the help of the capillary wicking effect. After the evaporation of the ethanol, several droplets of low-surface-tension Krytox GPL 103 (γ =16–20 mN/m) were dripped onto the membrane to wick into the pores of the PTFE to form a SLIPS layer. All the samples were placed horizontally on a flat table for about 12 hours to allow spontaneous impregnation of lubricant prior to any experimental characterization or measurement.

Fabrication of ITO-based LA-TEG

To fabricate the ITO-based LA-TEG, a piece of ITO glass slide was first ultrasonically cleaned in acetone and ethanol for 10 min, respectively. Then we gently covered a porous PTFE membrane onto the ITO glass followed by rubbing the membrane with the nitrile butadiene rubber for a charging treatment. Then we dropped several droplets of lubricants onto the charged membrane to fabricate the SLIPS layer. After that, a tapered aluminum electrode was attached to the SLIPS layer to construct the transistor-like electrode architecture. For comparison, we fabricated a control sample without the infusion of the lubricant using the similar method. Also, we fabricated a SLIPS-TENG without the infusion of the lubricant but without attaching the aluminum electrode.

Characterization and Electrical Measurement.

The optical transmittance was measured by using Perkin Elmer Lanbda 35 UV-VIS Spectrometer. Fourier-transform infrared (FT-IR) spectra were recorded using a Bruker Tensor 27 FT-IR Spectrometer with the attenuated total reflectance (ATR) accessory at a resolution of 4 cm^{-1} in the range of 4000-600 cm^{-1}.

We utilized a syringe pump and a plastic tube to form waterjet with the untreated tap water if there is no special instruction. The inner diameter of the plastic nozzle connecting to the outlet of the plastic tube is 1.65 mm, and the corresponding water droplet volume is 50 μL. If not specified, the substrate tilt angle and the release height of water droplet were fixed at 45° and 12 cm, respectively. The impact dynamic wetting behaviors of water droplets were recorded by a high-speed camera (Photron FASTCAM SA4) at a rate of 6,000 frame per second. An oscilloscope (Rohde and Schwarzrte, RTE1024) with a high-impedance (10 MΩ) probe was used for measuring the voltage output of all the devices. We measured the current and transferred charge using a low-noise current preamplifier (Stanford Research System Model SR570) or a nanocoulomb meter (Monroe model 284) coupled with the oscilloscope, respectively. Specially, for testing the behavior of TENGs at low temperature, any sample (LA-TEG or control) was stuck to a thermoelectric cooling stage, that was used to precisely control the sample surface temperature. All the experiments were carried under the ambient relative humidity of 60% and ambient temperature of 25℃ except for the test of samples in low temperature of -2℃ and high humidity of 100%.

Calculation of energy conversion efficiency and power density

As for a PCB-based LA-TEG unit, an electrical energy E of 0.236 μJ can be generated under a falling droplet impact. The kinetic energy of the droplet E_d is 58.8 μJ ($E_d = mgh$, m = 50 mg, h = 12 cm). Thus, the energy efficiency of the device is 0.4%.

The output power density of LA-TEG unit is calculated as $P_s=I^2R/S$, where P_s, I, R and S represent the output power density, output current, the external resistance and the spreading area of a droplet impacting on LA-TEG, respectively. Noted that the spreading area of a impacting droplet (50 μL and releasing height of 12 cm) is around 1.78 cm^2 measured through the high-speed imaging.

Reference

1 Liang, Q., Yan, X., Liao, X. & Zhang, Y. Integrated multi-unit transparent triboelectric nanogenerator harvesting rain power for driving electronics. *Nano Energy* **25**, 18-25 (2016).

2 Jeon, S.-B., Kim, D., Yoon, G.-W., Yoon, J.-B. & Choi, Y.-K. Self-cleaning hybrid energy harvester to generate power from raindrop and sunlight. *Nano Energy* **12**, 636-645 (2015).

3 Lin, Z. H., Cheng, G., Lee, S., Pradel, K. C. & Wang, Z. L. Harvesting water drop energy by a sequential contact-electrification and electrostatic-induction process. *Advanced Materials* **26**, 4690-4696 (2014).

4 Xu, W. *et al.* A droplet-based electricity generator with high instantaneous power density. *Nature* **578**, 392-396 (2020).

5 Wu, H. *et al.* Charge Trapping-Based Electricity Generator (CTEG): An Ultrarobust and High Efficiency Nanogenerator for Energy Harvesting from Water Droplets. *Adv Mater* **32**, e2001699, doi:10.1002/adma.202001699 (2020).